



Optimizing cycling skinsuit design through an integrated wind-tunnel and CFD workflow

Thijs van Druenen ^{a,*} ID, Bert Blocken ^{b,c} ID

^a Building Physics and Services, Department of the Built Environment, Eindhoven University of Technology, P.O. Box 513, 5600 MB, Eindhoven, the Netherlands

^b Institute of Mechanical, Process and Energy Engineering, School of Engineering and Physical Sciences, Heriot-Watt University, Edinburgh, Scotland, United Kingdom

^c Building Physics & Sustainable Design, Department of Civil Engineering, KU Leuven, Leuven, Belgium

ABSTRACT

This paper explores the use of computational fluid dynamics (CFD) in the design of cycling skinsuits with varying surface roughness. Traditional skinsuit design involves a complex and time-consuming process by wind tunnel experiments. CFD could potentially offer an alternative for predicting the performance and designing rider-specific skinsuits, though accurately modelling fabric surface roughness is challenging. The study characterizes skinsuit fabrics based on an equivalent sand-grain roughness height (k_s) value derived from drag reduction measurements on cylinders covered with specific fabrics. Three skinsuits, created from these fabrics, are assessed on a full-scale cyclist mannequin. For two of the three suits, the calculated drag area is within 0.6 % of the wind tunnel (WT) results. In the case of the third suit, the deviation with the WT drag area is 1.6 %. The CFD simulations reveal valuable insights, such as the impact of including variable k_s values on the location of flow separation, the local distribution of skin friction and pressure drag, and their effects on the near flow field. The agreement between WT and CFD results suggests the potential of CFD for designing aerodynamically optimized skinsuits for individual riders, while further research is recommended to refine and validate this approach.

Nomenclature

(continued)

A	Frontal area	m^2	p	Static pressure	Pa
C_D	Drag coefficient	—	p_0	Reference static pressure	Pa
C_{DA}	Drag area	m^2	r	Cylinder roughness	—
C_f	Skin friction coefficient	—	RANS	Reynolds-Averaged Navier-Stokes	
C_{fA}	Integration of shear stress distribution in the riding direction	m^2	Re	Reynolds number	—
CFD	Computational fluid dynamics		Re_{crit}	Critical Reynolds number	—
C_p	Pressure coefficient	—	Re_θ	Momentum thickness Reynolds number	—
C_{pA}	Integration of static pressure distribution in the riding direction	m^2	RMSE	Root mean squared error	%
C_s	Roughness constant	—	SST	Shear Stress Transport	
D	Cylinder diameter	m	T-SST	Transition Shear Stress Transport	
E	Model constant	—	TT	Time trial	
F_D	Drag force	N	t_x	Tangential vector to the surface projected on the riding direction	—
F_R	Fabric with rough surface finish		U	Magnitude of local velocity vector	m/s
F_R	The RMSE between $\Delta_{CFD,D}$ considering both turbulence models and $\Delta_{WT,D}$ through the application of F_R .	%	U_c	Riding velocity	m/s
F_S	Fabric with smooth surface finish		U_{crit}	Critical velocity	m/s
F_S	The RMSE between $\Delta_{CFD,D}$ considering both turbulence models and $\Delta_{WT,D}$ through the application of F_S .	%	U_p	Velocity at the cell centroid	m/s
k	Height of the roughness element	m	U_r	Velocity ratio	—
k_s	Equivalent sand-grain roughness height	m	U_{rel}	Relative velocity	m/s
K_s^+	Dimensionless roughness height	—	U_τ	Friction velocity	m/s
L	Characteristic length scale	m	V	Free-stream air velocity	m/s
N	Number of evaluated cylinder diameters	—	WT	Wind tunnel	
n_x	Normal vector to the surface projected on the riding direction	—	y^+	Virtually shifted dimensionless wall distance	—
			y^+	Dimensionless wall distance	—
			z_p	Microscope focus height	m
			γ	Intermittency	—

(continued on next column)

(continued on next page)

* Corresponding author.

E-mail address: t.v.druenen@tue.nl (T. van Druenen).

(continued)

ΔB	Downward shift of the logarithmic velocity profile near the wall	–
δC_D	Percentage drag change in C_D relative to the C_D obtained on the smooth (for CFD: $k_s = 0$ m) or uncovered (for WT: $k = 10 \mu\text{m}$) cylinder.	%
$\delta C_{D,\text{CFD}}$, D	Computed drag change at D in C_D for the respective k_s value compared to the case where $k_s = 0$.	%
$\delta C_{D,\text{WT}}$, D	Measured drag change in C_D for the cylinder with diameter D covered with a given fabric compared to the uncovered cylinder.	%
κ	Von Kármán constant	–
μ	Dynamic air viscosity	kg/ms
ν_w	Near-wall kinematic viscosity	m^2/s
ρ	Air density	kg/m^3
τ_w	Wall shear stress	N/m^2

1. Introduction

Reducing aerodynamic drag is one of the most important issues in high speed sports, such as cycling, speed skating and skiing. In cycling above speeds of 40 km/h in calm weather and over level terrain, the aerodynamic drag contributes to 90 % or more of the total resistance, about 70 % of which is due to the rider (Grappe et al., 1997; Kyle and Burke, 1984; Lukes et al., 2005). As the winning margins can be very narrow, sometimes a few hundreds of a second, even very small reductions in drag can make the difference. The aerodynamic drag is defined as:

$$F_D = \frac{1}{2} \rho U_{\text{Rel}}^2 A C_D \quad (1)$$

where ρ denotes the air density, U_{Rel} denotes the relative velocity, A is the frontal area of the body in the flow and C_D is the drag coefficient of the body. When maintaining the velocity within the same environmental conditions, a cyclist can reduce its drag by reducing its frontal area A , i. e. by changing its posture on the bike (e.g. Zdravkovich et al., 1996; Defraeye et al., 2010b; Barry et al., 2015a; Blocken et al., 2018a; van Druenen and Blocken, 2023) or by reducing the drag coefficient C_D . One method to reduce C_D is the application of cycling skinsuits, composed of fabrics, primarily with a specific roughness at designated zones of the suit. In the literature, drag reductions of more than 6 % were reported due to the use of skinsuits featuring zoned fabrics, compared to skinsuits with a smooth fabric for the trousers part and a rough fabric for the entire upper body (Brownlie et al., 2009).

Understanding the complex flow topology around a cyclist, with various regions of flow separation, can be challenging. Detailed investigations on flow topology have been performed by Griffith et al. (2014); Crouch et al. (2014); Jux et al. (2018) and Spoelstra et al. (2019). To gain insights into the relationship between flow topology and the potential drag reduction by a skinsuit fabric, one approach is to approximate different parts of a cyclist's body with geometrically simplified bluff bodies like cylinders (Chowdhury et al., 2010). This simplification is often employed in the initial stages of wind tunnel (WT) tests to evaluate the aerodynamics of fabrics used in a skinsuit (e.g., Brownlie et al., 1991; Kyle et al., 2004; Chowdhury et al., 2010; Oggiano, 2010; Underwood and Jermy, 2011). Subsequently, the aerodynamics of the complete skinsuit can be assessed on real athletes or mannequins.

The investigation of flow patterns around cylinders has been thoroughly explored in the past, as evidenced by studies such as Fage and Warsap (1929), Achenbach (1971), and Zdravkovich (1997). These studies have led to the elucidation of various flow regimes for a smooth cylinder subjected to crossflow at different Reynolds numbers $Re = \rho L V / \mu$ where L is a reference length set equal to the cylinder diameter, V the free-stream air velocity and μ is the dynamic viscosity of the air. In disturbance-free flows each flow regime occurs in a specific range of Re . In the subcritical regime ($350 < Re < 3 \times 10^5$), the flow in the boundary

layer is still laminar and separates at about 82° from the upstream stagnation point at the cylinder surface, while flow transition takes place in the shear layer downstream of the separation point. Consequently, an unsteady wake forms that exceeds the cylinder's diameter, and a fully turbulent vortex street develops. The vortex shedding induces an oscillating lift force on the cylinder, acting perpendicular to the flow direction. The C_D is about 1.2 (Zdravkovich et al., 1996).

As Re increases, the transition shifts from the shear layer to the boundary layer region. This transition involves a momentary separation of the shear layer, leading to a shift from laminar to turbulent flow. The higher energy in the turbulent shear layer allows it to reattach downstream along one side of the cylinder, reducing the wake width and lowering C_D . Initially, an asymmetrical pressure distribution emerges, characterized by the formation of a laminar separation bubble that creates suction on one side of the cylinder, inducing a steady flow circulation (Zdravkovich et al., 1996). At about $3.8 \times 10^5 < Re < 10^6$, C_D experiences a maximum reduction to about $C_D = 0.2$ as two laminar separation bubbles form in the boundary layer on each side of the cylinder. This is followed by flow transition and reattachment of the layers to both sides of the cylinder. After the reattachment, the flow separates again at around 140° (Achenbach, 1968), generating a highly turbulent wake with more irregular vortex shedding, narrower than the cylinder diameter. The phenomenon causing the sudden drop in C_D is known as the "drag crisis" and the Re at which the minimum C_D occurs is called Re_{crit} , the critical Re . In cycling, this is referred to as the so-called critical velocity U_{crit} , the relative velocity at which the local wake width is minimal (Terra et al., 2020).

Subsequently, C_D experiences a gradual increase, with a lower gradient, to about 0.54–0.70. As Re rises further, boundary layer transition occurs before the separation point. However, the flow separation still occurs at the back of the cylinder, resulting in a wake narrower than the cylinder diameter (Zdravkovich et al., 1996). Additionally, the turbulent vortex street that characterized the subcritical regime re-establishes, maintaining an unsteady wake structure.

Terra et al. (2020) explored the distribution of U_{crit} for various body segments of a non-pedalling cycling mannequin using robotic volumetric Particle Image Velocimetry. Their findings revealed that for the fully stretched leg, U_{crit} for the upper leg (inclination angle $\approx 72^\circ$) was below the typical cycling velocity of 15 m/s, while U_{crit} exceeded 15 m/s for the lower leg (inclination angle $\approx 5^\circ$), knee and for the mid-arm regions. It is important to note that in actual flows, flow regimes may manifest themselves in different Re ranges and may be suppressed due to the presence of disturbances. These disturbances are influenced by various parameters such as freestream turbulence, pressure gradients, surface roughness, surface temperature, surface curvature, and more.

The rationale behind utilizing rough skinsuit fabrics in cycling lies in the ability to modify surface roughness and the nature of the boundary layer at those surfaces, thereby shifting flow regimes to different Re and ultimately reducing C_D at the target relative velocity. Achenbach (1971) conducted experiments with circular cylinders in crossflow, demonstrating that by covering the cylinder with emery paper, the separation points of the flow at a given Re number could be delayed from around 82° to 120° .

The use of rough textiles on fabric-covered cylinders has demonstrated the ability to facilitate the drag crisis, lowering drag by up to 50 % and shifting the minimum drag to lower Reynolds numbers (Brownlie et al., 1991, 2009; Brownlie, 1992). Skinsuits incorporating these textiles could reduce cyclist drag, with a 6.3 % (Brownlie et al., 2009) and 7 % (Brownlie et al., 1991; Brownlie, 1992) difference between the best and worst performers among the tested suits. The evaluations were conducted on pedalling cyclists, noting that the suits featured fully covered arms and both covered (Brownlie et al., 1991; Brownlie, 1992) and uncovered (Brownlie et al., 2009) lower legs, and excluded the use of gloves and overshoes. The disparity in drag reduction (up to 50 % on cylinders and up to 7 % on real cyclists) was attributed to the complex geometries of the human body and bicycle, hindering surface

roughness-induced flow transition (Brownlie et al., 1991, 2009). Kyle et al. (2004) and Brownlie et al. (2009) introduced the use of different fabrics for specific areas: rough fabrics on limb segments reduced the form drag by anticipating flow transition, while smooth fabrics in zones with attached airflow, such as the torso, reduced skin friction. During WT measurements, these new zoned time trial (TT) skinsuits showed drag reductions of up to 3.9 % while the cyclist was pedalling and up to 6.3 % while the cyclist was not pedalling, compared to older versions composed of only one or two fabrics. In the two-fabric versions, a smooth fabric was used for the trousers part and a rough fabric for the entire upper body. Moreover, the new track skinsuit, optimized for a distinct posture, arm position, and higher velocities, achieved a 6.3 % reduction in drag compared to TT skinsuits while pedalling (Brownlie et al., 2009).

The current state-of-the-art in practical development of a skinsuit involves an extensive process of testing, trial and error, primarily drawing upon the manufacturer's and designers' experience. This process is expensive and highly time-consuming. Furthermore, the optimal suit for one cyclist may not necessarily yield the same performance for another, as the precise positioning of rough textiles depends on the local U_{crit} (Terra et al., 2020), where U_{crit} is influenced by various factors including the cyclist's morphological characteristics, posture, equipment, and other variables. However, it's often impractical and cost-prohibitive to have each individual cyclist undergoing the costly process of visiting a WT for suit optimization. An alternative solution may lie in the application of computational fluid dynamics (CFD), a technique widely employed in the cycling industry (e.g. British Cycling, 2018; Davis, 2022) and in the scientific literature (Crouch et al., 2017; Malizia & Blocken, 2020a, 2021).

Historically, the main method in CFD for evaluating the effects of surface roughness on drag is based on the equivalent sand-grain roughness height (k_s), a representative height of the roughness elements normal to the wall which can also be expressed as the dimensionless roughness height:

$$K_s^+ = \rho k_s U_\tau / \mu \quad (2)$$

with U_τ the friction velocity. It was first proposed by Schlichting (1936), and is an empirical model in which rough surfaces with various features are compared to data from Nikuradse (1933) concerning flow in pipes with varying sizes of sieved sand glued to the wetted surface. Rough surfaces were assigned a value of k_s based on comparisons with Nikuradse's data, using empirical correlations derived from experiments. Nikuradse found that, by increasing k_s , the wall shear stress and the mean velocity gradient near the wall increased.

To account for the additional shear from the roughness, the standard law of the wall is modified with ΔB , which represents a downward shift of the logarithmic velocity profile near the wall (Hama, 1954; Cebeci and Bradshaw, 1977). In the following equations, the implementation from the CFD code ANSYS (2021a) is adopted, which was used for the simulations in the present article:

$$\frac{U_p U_\tau}{\tau_w / \rho} = \frac{1}{\kappa} \ln(Ey^+) - \Delta B \quad (3)$$

With U_p the mean velocity at the cell centroid, τ_w the wall shear stress, E a model constant that equals 9.973 and y^+ the dimensionless wall distance that is defined as:

$$y^+ = \frac{\rho y_p U_\tau}{\mu} \quad (4)$$

Depending on the dimensionless roughness height, ΔB can be split into three distinct regions. A surface is defined as hydrodynamically smooth when $K_s^+ < 2.25$, which means that the size of the roughness element is smaller than the viscous sub-layer at the surface and ΔB will be 0. If $K_s^+ > 90$ the height of the roughness elements are much larger than the

thickness of the viscous sub-layer, then the boundary is called hydrodynamically rough and ΔB is calculated as:

$$\Delta B = \frac{1}{\kappa} \ln(1 + C_s K_s^+) \quad (5)$$

Where C_s is a roughness constant, usually kept at its default value of 0.5. A transitional regime is present for $2.25 \leq K_s^+ \leq 90$ and ΔB is expressed as:

$$\Delta B = \frac{1}{\kappa} \ln \left(\frac{K_s^+ - 2.25}{87.75} + C_s K_s^+ \right) \sin(0.4258(\ln K_s^+ - 0.811)) \quad (6)$$

In the CFD code, roughness is taken into account by adjusting the near-wall kinematic viscosity ν_w (ANSYS, 2021a). First K_s^+ and y^+ are calculated. Maintaining an appropriate y^+ value is crucial for accurate modelling of the near-wall region. A low y^+ value, typically less than 5, is recommended to ensure that the viscous sublayer and buffer layer are adequately resolved. Note that when the centre of the near-wall cell height y_p is smaller than k_s , the wall is virtually shifted to half the dimensionless height of the roughness element (ANSYS, 2021a), so that:

$$y^+ = y^+ + \frac{K_s^+}{2} \quad (7)$$

Next, ΔB is calculated with either equation (5) or (6), after which E' is calculated with

$$E' = \frac{E}{\exp(\Delta B)} \quad (8)$$

Then, ν_w is calculated accordingly;

$$\nu_w = \frac{\mu y^+}{\frac{1}{\kappa} \rho \ln(E'y^+)} \quad (9)$$

after which the momentum and pressure equations are solved. Note that while the general approach of modelling surface roughness via ΔB is commonly used in CFD, the specific implementation presented here, including the exact formulation of ΔB and the adjustment of y^+ and ν_w , is particular to ANSYS Fluent (ANSYS, 2021a) and may differ in other codes.

The roughness implementation in the ANSYS (2021a) CFD code is defined by k_s or K_s^+ and the roughness constant C_s . Modelling the effect of surface roughness is challenging, as correlations that accurately relate actual surface roughness to k_s and C_s are rarely known. In most real-life conditions, k_s tends to function as a dynamic flow variable rather than a static geometric one. Consequently, for any new rough surface or geometry, k_s must be determined either from existing data or through new experiments.

The past few decades, a large amount of work has been devoted to determining k_s . Empirical correlations for the calculation of k_s were outlined by several review papers (e.g. Flack and Schultz, 2014; Kadivar et al., 2021) and it was found that methods using only a single parameter or height (e.g. arithmetic mean deviation, root-mean-square roughness, skewness, peak-to-valley height, etc.) were unsuccessful in modelling flows over rough surfaces. Surface flows over various types of roughness were evaluated, including sprayed paint, sandpaper, woven meshes, packed spheres, pyramids, bars, etc. Nevertheless, it was found that no single roughness length scale could characterize all roughness types across all roughness regimes, complicating the selection of an appropriate correlation for k_s .

In recent years, the application of Direct Numerical Simulation (DNS) has gained traction, with several studies utilizing DNS to establish correlations between surface properties and their impact on ΔB (Chan et al., 2015; Thakkar et al., 2017; Forooghi et al., 2017). More contemporary approaches involve the application of neural networks and machine learning methods. Numerous studies have utilized these techniques to develop a predictive model for k_s based on a

comprehensive set of DNS studies involving various rough surfaces (Jouybari et al., 2021; Lee et al., 2022; Yang et al., 2023). These models have shown the ability to predict k_s for rough-wall turbulent flows with an average error of approximately 10 %. A detailed overview is available in the review papers by Kadivar et al. (2021), Chung et al. (2022), and Flack and Chung (2022).

While much of the work is rooted in pipe-flow or zero-pressure gradient flows over flat plates, studies on cycling skinsuits often consider the cyclist as an assembly of cylinders. To characterize the surface roughness of skinsuit fabrics on cylinders, various methods have been identified in the literature (Oggiano et al., 2013). Hoerner (1965) and Achenbach (1971) highlighted the k/D ratio (height of roughness element k to cylinder diameter D) as crucial for determining Re_{crit} . Other approaches involve models based on surface topology parameters like protrusion width and depth (Oggiano et al., 2007; Oggiano and Sætran, 2009; Underwood and Jermy, 2011), wale-related measurements (Oggiano et al., 2009a, 2009b) or the integral measurements of fabric surface profiles (Brownlie, 1992; Chowdhury, 2012; Moria, 2013). However, Oggiano et al. (2013) noted limitations in accurately describing fabric surface topology with these models due to the limited number of parameters. In addition, Kyle et al. (2004) and Brownlie et al. (2009) measured fabric properties like roughness, stretching, coating, permeability, and thickness, but they found no precise correlation between these properties and the fabrics' aerodynamic performance. Chowdhury and Alam (2014) employed a scanning electron microscope to characterize ten fabrics based on the arithmetic mean roughness over the measured surface. They identified an inversely proportional relationship between k/D and Re_{crit} for most samples. However, alterations in parameters other than arithmetic mean roughness, such as coating and a shift from knitted to woven textures, led to deviations from the established relationships. In a study by Hsu et al. (2019), WT measurements were conducted on a cylinder using 38 different fabrics. The ten-point height parameter, derived from 3D laser micro scanning and encompassing the sum of the average of the height/depth of the five highest peaks and five deepest valleys, was utilized for fabric characterization. Empirical correlations curves were established for Re_{crit} and minimum C_D values. Notably, considerable scattering of data points was observed around the correlation curves, which the authors attributed to differences in woven and knitted texture patterns.

Previous studies have demonstrated the drag reduction potential of skinsuits made from various fabrics (Kyle et al., 2004; Brownlie et al., 2009). However, since the process of creating and testing these skinsuits in wind tunnels is typically costly and time-consuming, the present authors are investigating the possibility of implementing surface roughness modelling in CFD to predict the performance of skinsuits made from different fabrics. However, accurately representing specific roughness textures in CFD surface roughness modelling poses a significant challenge. To the best of the authors' knowledge, the numerical prediction and experimental validation of the performance of a cycling skinsuit made of several fabrics has not yet been published in the literature. Therefore, this study proposes an integrated WT and CFD workflow for rider-specific skinsuit design, and evaluates its predictive capability by comparing CFD results obtained using the ANSYS Fluent CFD code with wind tunnel measurements.

The initial phase of this study involves acquiring drag values through WT tests on cylinders covered with two distinct fabrics; one relatively smooth and the other rough. Subsequently, CFD simulations are employed to identify the k_s value that yields a comparable drag reduction. In the subsequent phase, the performance is evaluated using a full cyclist mannequin. The computational geometry of the cyclist is segmented to align with the actual stitching pattern of the skinsuit, with predetermined k_s values assigned to different fabric surface zones. Simulations are conducted for three skinsuit variants, and the results are validated with WT measurements.

2. Methodology

The starting point for this study is the determination of the k_s values to represent the skinsuit fabrics aerodynamic behaviour at a cycling velocity of $U_c = 15$ m/s in the absence of head, tail or crosswinds, which is often used as reference velocity in TT studies (Blocken et al., 2013, 2018b; Terra et al., 2020). Therefore, WT experiments are conducted to determine the drag coefficients of three different cylinders covered with one of two different fabrics, a rough and a smooth one, across a range of velocities. The obtained drag coefficients are expressed as a percentage in comparison to the drag coefficient of the uncovered cylinder.

Following this, 2D CFD simulations are executed for the three cylinder diameters at a reference velocity of 15 m/s while varying the roughness parameter (k_s) over a wide spectrum. The objective here is to identify a specific k_s value that yields a similar percentage drag compared to the two fabrics tested in the WT.

Next, the fabrics and the associated roughness values are evaluated using a full skinsuit on a test mannequin. The test mannequin's computational geometry is divided into various segments that align with the stitching pattern of the actual skinsuit. This segmentation allows each surface to be assigned the pre-determined k_s value corresponding to either the rough or the smooth fabric. Finally, 3D CFD simulations are conducted for the mannequin with the three different skinsuit variants, which are subsequently validated with WT measurements. These skinsuits used in the WT experiments are created from the two fabrics that were assessed earlier. To allow a direct comparison, both CFD simulations and WT measurements are performed with static legs, aligning with common WT skinsuit testing methods using static mannequins (Barry et al., 2015; Brown et al., 2023; Blocken and Malizia, 2024; Blocken et al., 2021, 2024; Grouch et al., 2017; Malizia & Blocken, 2020a, 2021; van Druenen and Blocken, 2023).

3. Establishing a roughness correlation

WT experiments are conducted to determine the drag coefficients of the cylinders with three different diameters, covered with two sleeves of fabrics, a rough and smooth one, across a range of free-stream velocities. When dealing with cylinders covered with roughness, the surface topology of the fabric doesn't scale proportionally with the cylinder diameter. This lack of proportionality is indicated by the cylinder roughness $r = k/D$. Consequently, cylinders with $D = 0.075$ m, 0.11 m, and 0.16 m are utilized to simulate various regions of a cyclist's body limbs.

The drag coefficients obtained from the experiments are presented as a percentage relative to the drag coefficient of the uncovered and relatively smooth steel cylinder; without any fabric sleeve. Subsequently, 2D steady RANS CFD simulations are conducted for the three cylinders, maintaining a reference velocity of $U_c = 15$ m/s, while systematically varying the computational roughness parameter (k_s) across a broad range. The assessment involves employing two different turbulence models.

3.1. Wind tunnel cylinder tests

The two applied fabrics were provided by a leading cycling skinsuit manufacturer and selected for their anticipated different aerodynamic behaviour, due to significant variations in surface properties: a relatively smooth fabric referred to as F_S and a comparatively rough fabric denoted as F_R , as depicted in Fig. 1. Macroscopic examination reveals a predominantly smooth surface for F_S (Fig. 1a), whereas F_R exhibits a pattern of embedded circles (Fig. 1d). Microscopic analysis is performed with a Zeiss Axio imager 2 microscope, and highlights the woven, closed structure of F_S and the knitted, porous structure of F_R , as shown in Fig. 1b and e, respectively. The sensor focus height is denoted by z_p . Height maps (Fig. 1c-f) are generated by focus stacking microscopic images at various z_p values, facilitating the approximation of the

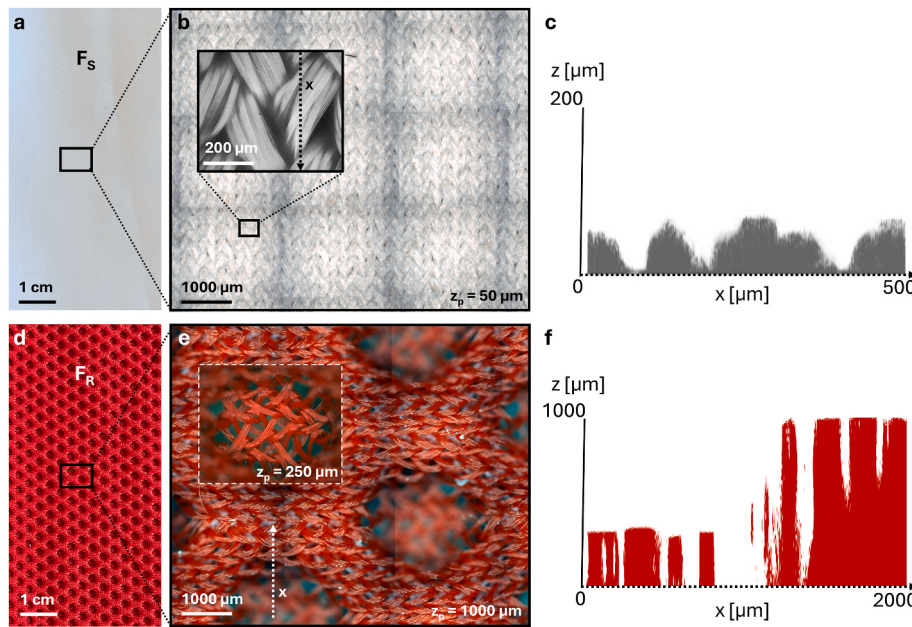


Fig. 1. (a,d) Macro and (b,e) micro photographs with focus on $z = z_p$, with (c,f) corresponding height maps, comparing F_S (a–c) and F_R (d–f) samples.

roughness element height k , with values of $k = 60 \mu\text{m}$ for F_S and $k = 720 \mu\text{m}$ for F_R . This is in accordance with the regulations by the International Cycling Union, which state that the surface roughness of cycling skinsuits should not exceed $k = 1 \text{ mm}$ (UCI, 2024). Three sleeves are tailored for each fabric to cover specific cylinder diameters without subjecting the fabric to excessive stretching. For cylinder diameters of $D = 0.075 \text{ m}$, 0.11 m , and 0.16 m , this yields r values of 8.0×10^{-4} , 5.5×10^{-4} , and 3.8×10^{-4} , respectively, for F_S , and r values of 9.6×10^{-3} , 6.5×10^{-3} , and 4.5×10^{-3} , respectively, for F_R .

3.1.1. Wind tunnel setup

The WT measurements take place in the closed-section WT at Eindhoven University of Technology in the Netherlands. The test section has a cross-sectional area of $3 \times 2 \text{ m}^2$ (width x height), with reference velocities ranging from 0 to 30 m/s . The 1.85 m long cylinders are made of S235 steel with an approximated k value of about $10 \mu\text{m}$ (Mebarek et al., 2024). During the tests, the vertical cylinder is positioned on a two-component force balance integrated into an elevated turntable as shown in Fig. 2. The measurements are performed at wind velocities ranging from 2 to 30 m/s , with a 1 m/s interval. The stitch of the sleeve is located on the leeward side of the cylinder. The air velocity is measured with a pitot-static tube. All results have been corrected to account for differences in temperature, atmospheric pressure and relative humidity observed during the measurements, to a standard sea-level atmospheric pressure and air density of 1.225 kg/m^3 at 15°C .

3.1.2. Wind tunnel results

The WT measurement results are presented in Fig. 3. In this figure, the vertical dashed line signifies Re where the free-stream velocity V equals the target “riding” velocity of 15 m/s . Across all cylinder diameters (D), it is evident that the drag crisis is not observed for the uncovered cylinder. This observation aligns with the drag regimes defined by Zdravkovich (1997), which situate the occurrence of the drag crisis on a smooth cylinder somewhere within the range of $3.8 \times 10^5 < Re_{\text{crit}} < 10^6$.

When the sleeve with F_S is applied, Re_{crit} occurs for $D = 0.16 \text{ m}$ at approximately 3.5×10^5 . For $D = 0.11 \text{ m}$, the initiation of the critical regime is apparent, while for $D = 0.075 \text{ m}$, there is no discernible drop in C_D . When the sleeve with F_R is employed, Re_{crit} is observed for all cylinder diameters. For $D = 0.16 \text{ m}$ and $D = 0.11 \text{ m}$, Re_{crit} equals 10^5 ,



Fig. 2. Wind tunnel setup showing the mounted cylinder ($D = 0.16 \text{ m}$) with F_S , and the pitot-static tube location.

whereas for $D = 0.075 \text{ m}$, Re_{crit} equals 7×10^4 . Notably, for both $D = 0.075 \text{ m}$ and $D = 0.11 \text{ m}$, Re_{crit} aligns closely with the Reynolds number corresponding to U_c . This correlation is likely not coincidental, as the selection of this fabric was informed by the manufacturer’s extensive experience and its proven effectiveness in real skinsuit applications.

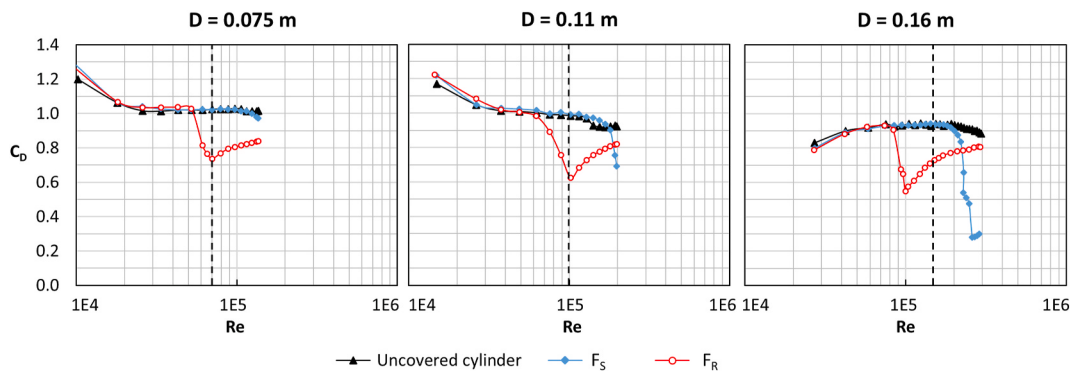


Fig. 3. Wind tunnel results for cylinder tests, with vertical dashed line denoting where the free-stream velocity V equals the simulated riding velocity U_c .

3.2. CFD cylinder tests

3.2.1. Computational geometry and domain

The 2D computational domain is illustrated in Fig. 4 and was determined by following best practice guidelines for 3D CFD simulation of urban flows (Franke et al., 2007; Tominaga et al., 2008; Blocken, 2015) and 2D CFD simulation of wind turbine flows (Rezaieha et al., 2017, 2018). The dimensions are 8 m (length) \times 3 m (width). The width of 3 m is taken equal to the width of the WT. The distance of the centre of the cylinder to the inflow of the domain is 2 m, and the distance of the centre of the cylinder to the outlet of the domain is 6 m. A maximum blockage of 5.3 % is present for the largest cylinder diameter $D = 0.16 \text{ m}$.

3.2.2. Computational grid and grid-sensitivity analysis

The computational grid is established following a grid-sensitivity analysis, involving the creation of three grids for $D = 0.16 \text{ m}$ and $k_s = 0$ at the surface of the cylinder. The medium grid features a surface cell length of 1 mm along the cylinder circumference and a y_p value of 0.01 mm, in line with the grid characteristics of the full-cyclist grid (as will be detailed in subsection 4.2.3) and determined in an earlier study (van Druenen and Blocken, 2024). Subsequently, the grid underwent systematic refinement or coarsening to produce the Fine and Coarse grids (see Fig. 5). The distinctive characteristics of these grids, along with the outcomes of the grid-sensitivity analysis, can be found in Table 1 and section 3.3.1.

3.2.3. Other computational settings

The CFD simulations are performed using the 2D steady RANS equations that are solved using the commercial CFD code ANSYS Fluent 21.1 (ANSYS, 2021b). Since wall functions are often unreliable in predicting the location of flow separation (Casey and Wintergerste, 2000), they are not employed in this study. Instead, the flow is fully resolved

down to the viscous sublayer. Two turbulence models, each with a different transition model, are evaluated: one using the shear stress transport (SST) $k-\omega$ turbulence model and the γ -transition model, and the other using the transition shear stress transport (T-SST) turbulence model with the γ - Re_0 transition model.

The SST $k-\omega$ model (Menter, 1994) is a two-equation eddy-viscosity model that combines the use of a $k-\omega$ formulation in the near-wall region and switches to $k-\epsilon$ behaviour in the free-stream. Low-Re corrections are applied, and the γ -transition model (Menter et al., 2015) is used to improve the prediction of large-scale separation and reattachment of the flow in the boundary layer. This model solves a transport equation for macro-scale turbulence intermittency, and the transition momentum thickness Reynolds number, which determines the transition onset criteria, is calculated locally based on local flow conditions. Pressure-velocity coupling is performed with the Coupled algorithm. Pressure interpolation is second order and second order upwind schemes are applied for the equations of momentum, turbulent kinetic energy and specific dissipation rate. The Least Squares Cell Based method is used to compute gradients. The pseudo-transient solver is applied with automated time step sizing. Drag values are averaged over 5000 iterations after a number of 1000 iterations are performed for initialization of the flow field.

The T-SST model (Menter et al., 2006a, 2006b) is based on the coupling of the SST $k-\omega$ transport equations with two additional transport equations for the intermittency γ and momentum thickness Reynolds number Re_0 to track transition onset criteria. In the present study, the T-SST model is employed with roughness correlation and production limiters (ANSYS, 2021b). Pressure-velocity coupling is performed using the Coupled scheme, and pressure interpolation is conducted with second-order accuracy. Second-order upwind discretization schemes are employed for both the convection and viscous terms of the governing equations. Gradients are computed using the Least Squares Cell Based scheme. Pseudo-transient under-relaxation is applied, with a total of

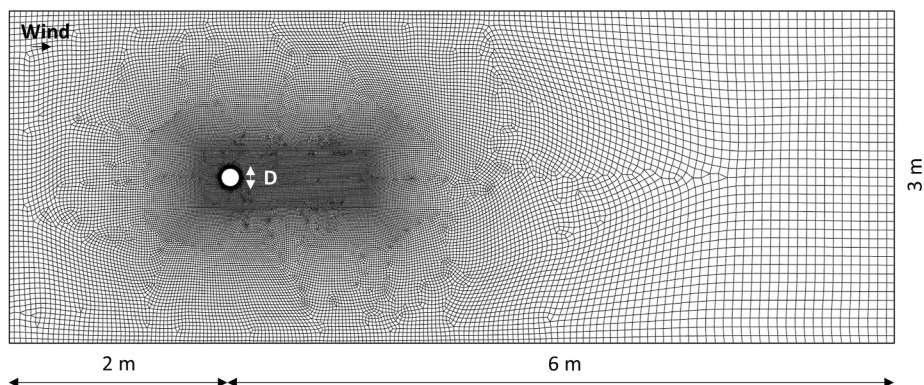


Fig. 4. 2D computational grid; medium grid with 58,869 cells.

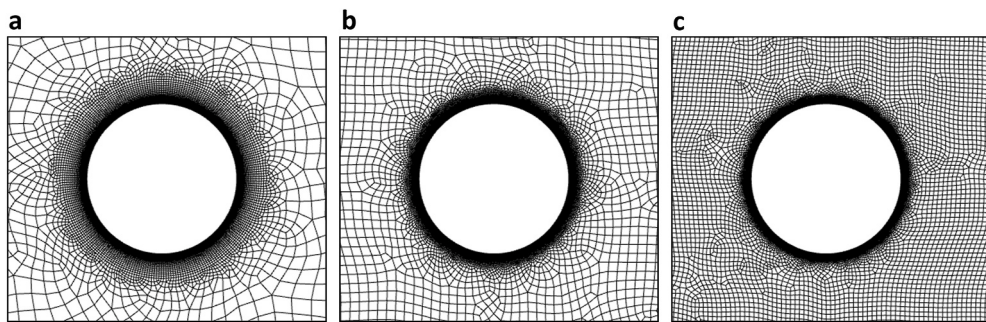


Fig. 5. 2D computational grids for (a) coarse grid with 35,258 cells, (b) medium grid with 58,869 cells and (c) fine grid with 169,368 cells.

Table 1

Grid characteristics for three different grids with calculated C_D and δC_D difference with respect to that on the finest grid.

	Surface cell length	y_P	Wall-adjacent Prism layers	Cells	$k-\omega$ SST	T-SST
	[mm]	[mm]	#	#	$C_D [-]$	Δ
Fine	0.75	0.0075	40	169,368	0.624	–
Medium	1	0.01	42	58,869	0.627	+0.5 %
Coarse	2	0.02	44	35,258	0.650	+4.2 %

6000 pseudo-transient time steps used in the simulations. Averaged drag values are obtained by averaging over the last 5000 time steps after a number of 1000 iterations for flow field initialization.

3.2.4. Boundary conditions

At the inlet of the computational domain, a uniform mean velocity of 15 m/s and a turbulence intensity of 0.5 % is enforced, to take into account the gradual decay of turbulence intensity to around 0.2 % observed at the measurement location, hence simulating the WT conditions at the measurement location. The surface of the cylinders is given a k_S value in the range of 0.01–10 mm. At the outlet, zero static gauge pressure is specified. At the lateral boundaries, a slip wall boundary condition is imposed.

3.3. Results

3.3.1. Grid sensitivity analysis

The results of the grid sensitivity analysis are evaluated in terms of the drag coefficient C_D and presented in Table 1. A comparison between the coarse and fine grid solutions reveals differences of 4.2 % and 0.2 % for the SST $k-\omega$ and T-SST models, respectively. The medium grid yields deviations of 0.5 % and 0.4 % compared to the fine grid for SST $k-\omega$ and T-SST, respectively. Since these discrepancies fall within an acceptable margin of uncertainty, the medium grid is selected for the remainder of the study.

3.3.2. Roughness correlation

For diameters $D = 0.075$ m, $D = 0.11$ m and $D = 0.16$ m, CFD simulations are performed at $Re = 7.6 \times 10^4$, 1.1×10^5 and 1.6×10^5 , respectively. These simulations are aligned with condition $V = U_c = 15$ m/s, as indicated by the dashed lines in Fig. 3. The CFD simulations are represented by solid lines as a function of k_S (Fig. 6a and b) and k_S/D (Fig. 6c and d). The dotted and dashed lines represent the results of the WT measurements for F_S and F_R at U_c (as detailed in subsection 3.1.2). These lines serve as a visual guide for evaluating the agreement with the CFD results. The results are presented in terms of δC_D , defined as the percentage change in C_D relative to the C_D obtained on the smooth (for CFD: $k_S = 0$ m) or uncovered (for WT: $k = 10 \mu\text{m}$) cylinder. As this study attempts to simulate an inherently unsteady flow using a steady-state RANS approach with a pseudo-transient solver, certain limitations arise, particularly in the wake region. The unsteady vortex shedding is

numerically forced into a steady solution, leading to oscillations in the residuals and in several features of the flow field, such as separation points, rather than true convergence. This behaviour was found to be sensitive to turbulence model and k_S , and is therefore included in more detail in the following section.

Fig. 6a depicts δC_D obtained using the $k-\omega$ SST turbulence model as a function of k_S . The black solid line represents CFD simulations for $D = 0.16$ m, illustrating a pronounced non-monotonic behaviour. For $k_S < 0.2$ mm, δC_D decreases with increasing k_S to approximately –4 %, before rising to about +15 % at $k_S = 0.5$ mm. Subsequently, for $5 > k_S > 0.5$ mm, δC_D decreases rapidly with increasing k_S to approximately –26 %. δC_D reduces further to about –28 % for $10 > k_S > 5$ mm. Analysis of the CFD simulations indicates the presence of oscillating flow patterns for $k_S \leq 0.2$ mm, with separation points fluctuating between 80° and 105° . For $k_S \geq 0.5$ mm, a steady flow is observed, and the separation points shift from about 80° at $k_S = 0.5$ mm to approximately 120° at $k_S = 10$ mm. For $D = 0.11$ m and $D = 0.075$ m, represented by the red and blue solid lines respectively, variations in δC_D are small, within ± 2 %, for $k_S < 0.1$ mm. Flow analysis indicates an oscillating wake for $k_S < 0.1$ mm. Beyond $k_S > 0.1$ mm, a steady flow is present, and δC_D drops to –45 % for $D = 0.11$ m and –52 % for $D = 0.075$ m at $k_S = 10$ mm.

The results obtained using the T-SST turbulence model are presented in Fig. 6b. For $D = 0.16$ m, δC_D decreases with increasing k_S to approximately –6 % at $k_S = 0.2$ mm. Subsequently, with further increases in k_S , δC_D rises slightly to about –5 % at $k_S = 0.5$ mm, followed by a strong reduction to –24 % at $k_S = 5$ mm. Within the range of $10 > k_S > 3$ mm, δC_D varies slightly between –23 % and –26 %. For $D = 0.11$ m, δC_D decreases with increasing k_S to –21 % at $k_S = 3$ mm, maintaining a range between –17 % and –21 % for $10 > k_S > 3$ mm. Similarly, for $D = 0.075$ m, δC_D decreases with increasing k_S to –23 % at $k_S = 2$ mm, and remains within the range of –17 % to –23 % for $10 > k_S > 2$ mm. Unlike the $k-\omega$ SST model, the T-SST CFD simulations reveal the presence of oscillating flow patterns for all values of k_S . Specifically, for $k_S = 0$ mm, the separation point fluctuates between 75° and 105° . As k_S increases, the separation points shift backward, ranging between 82° and 105° at $k_S = 0.1$ mm, and to between 82° and 120° at $k_S = 10$ mm. As anticipated and depicted in Fig. 6c for $k-\omega$ SST and in Fig. 6d for T-SST, the calculated drag reduction across the evaluated parameters cannot be represented solely as a function of the nondimensional parameter k_S/D .

In an optimal scenario, one would be able to associate a single k_S value with a specific fabric, whether F_S or F_R , where the numerically

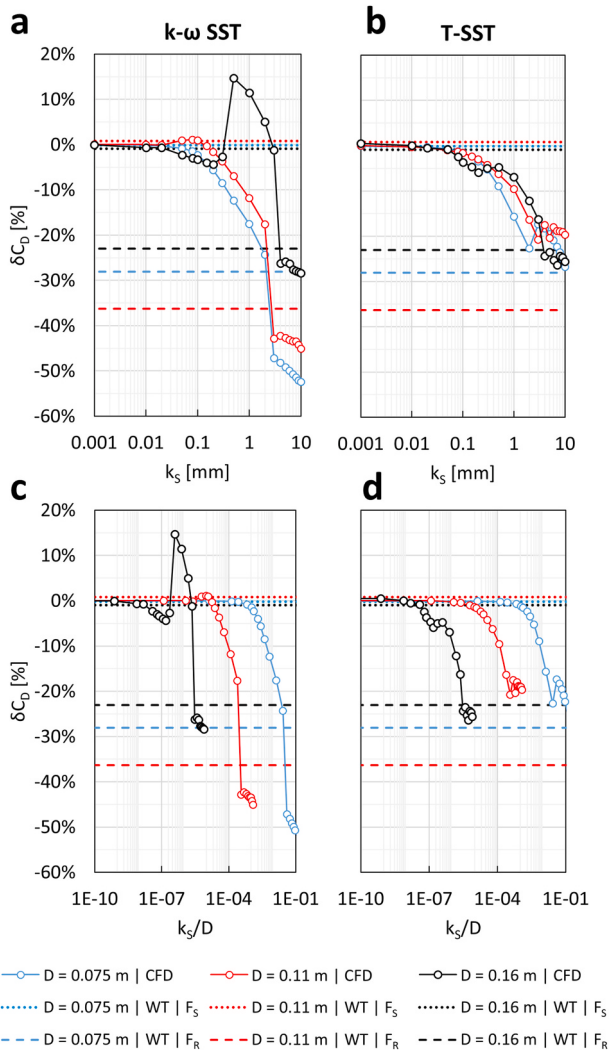


Fig. 6. C_D differences at 15 m/s between WT (F_S and F_R) and CFD simulations with varying (a,b) k_S and (c,d) k_S/D values using (a,c) $k\text{-}\omega$ SST and (b,d) T-SST, presented relative to WT uncovered and CFD zero roughness cylinder, respectively.

computed drag reduction compared to that of the smooth cylinder aligns with the corresponding WT results for all three cylinder diameters. In Fig. 6a and b, this alignment would be reflected by a close agreement among all three colours at a single k_S value for F_S , observed between the solid and dotted lines, and similarly at another k_S value for F_R , observed between the solid and dashed lines. However, there is no single k_S value that meets this criterion consistently across all three cylinders, particularly for F_R . To determine the single optimal k_S value for either F_S or F_R for all diameters, the root mean squared error (RMSE) is employed:

$$RMSE = \sqrt{\frac{\sum_{D=1}^N (\delta C_{D,CFD,D} - \delta C_{D,WT,D})^2}{N}} \quad (10)$$

with $N = 3$ the number of cylinder diameters D , $\delta C_{D,CFD,D}$ the computed change in C_D for the respective k_S value compared to $k_S = 0$ and $\delta C_{D,WT,D}$ the measured change in C_D for the cylinder covered with the respective fabric compared to the uncovered cylinder. The results are visualized in Fig. 7, where for the evaluated k_S values, the RMSE is plotted between the drag reduction obtained by each turbulence model and the drag reduction obtained in the WT by both fabrics. Additionally, the RMSE is plotted between the combined CFD results (for both turbulence models) and the WT results for either F_S and F_R , and denoted as \bar{F}_S and \bar{F}_R .

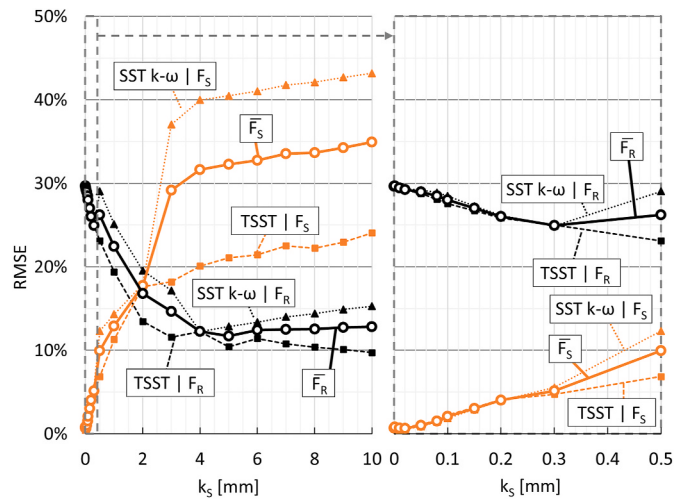


Fig. 7. Root Mean Squared Error (RMSE) related to the agreement between WT and CFD outcomes when employing various k_S values.

respectively.

For low k_S values the RMSE for F_S is relatively small, with $RMSE < 5\%$. For k_S values lower than 0.2 mm. For \bar{F}_S an RMSE of 1.0 % is found for $k_S = 0.05$ mm. The minimum RMSE values for F_R are higher. For SST $k\text{-}\omega$ and F_R the smallest value is found for $k_S = 4$ mm with $RMSE = 11.7\%$. For T-SST and F_R the lowest value is $RMSE = 9.7\%$ for $k_S = 10$ mm. For the combined results \bar{F}_R , the lowest RMSE = 11.7 % for $k_S = 5$ mm.

Based on \bar{F}_S and \bar{F}_R , $k_S = 0.05$ mm ($RMSE = 1.0\%$) is chosen for F_S , while $k_S = 5$ mm ($RMSE = 11.7\%$) is selected for F_R . This translates to k_S/D values of 6.7×10^{-4} , 4.5×10^{-4} and 3.1×10^{-4} , for $D = 0.075$ m, $D = 0.11$ m and $D = 0.16$ m, respectively. Table 2 presents δC_D of F_S relative to the uncovered cylinder for the WT results, and δC_D of $k_S = 0.05$ mm relative to $k_S = 0$ mm for the CFD results, at 15 m/s. However, for F_R , the larger RMSE makes it challenging to identify a single k_S value that accurately predicts the drag reduction on all three tested cylinders. Therefore, the evaluation of the full skinsuit in section 4 will be conducted using three different k_S values for F_R . In addition to $k_S = 5$ mm, values of $k_S = 1$ mm ($RMSE = 22.4\%$) and $k_S = 10$ mm ($RMSE = 12.8\%$) will be employed. Table 3 presents δC_D of F_R relative to the uncovered cylinder for the WT results, and δC_D of the respective k_S values relative to the smooth cylinder ($k_S = 0$ mm) for the CFD results, at 15 m/s.

4. Full skinsuit

In this section, the evaluation of fabric representations through their associated k_S values is performed using CFD, employing a full skinsuit on a cycling model. Furthermore, WT experiments are conducted on a full-scale mannequin wearing skinsuits made from these fabrics to validate the CFD simulations.

4.1. Wind tunnel skinsuit tests

4.1.1. Wind tunnel setup

Three variations of skinsuits are designed for assessment. All

Table 2

δC_D at 15 m/s for F_S .

D [m]	WT	CFD	
		$k_S = 0.05$ mm	
0.075	-0.20 %	-0.90 %	-0.70 %
0.11	0.80 %	0.90 %	-1.00 %
0.16	-0.90 %	-2.30 %	-0.80 %

Table 3 δC_D at 15 m/s for F_R .

D [m]	WT	CFD					
		k _S = 1 mm		k _S = 5 mm		k _S = 10 mm	
		SST k- ω	T-SST	SST k- ω	T-SST	SST k- ω	T-SST
0.075	-28 %	-18 %	-16 %	-49 %	-20 %	-52 %	-27 %
0.11	-36 %	-12 %	-10 %	-43 %	-20 %	-45 %	-20 %
0.16	-23 %	11 %	-7 %	-26 %	-24 %	-28 %	-26 %

skinsuits are divided into three zones, as shown in Fig. 8. Variants are produced by employing fabrics F_S and F_R in zone 1, 2, or 3, as outlined in Table 4. Zone 1 covers the upper leg area and the race number pocket. Zone 2 encompasses the lower and upper back areas. Zone 3 includes the lower and upper arms, shoulders, and chest area. In suit 1, F_S is applied in all zones. Suit 2 incorporates F_S in zone 1 and F_R in both zone 2 and zone 3. In suit 3, F_S is used in zone 1 and zone 3, while F_R is applied in zone 2.

The WT measurements are conducted in the open-section WT at Eindhoven University of Technology. In these experiments, a full-scale time trial bicycle and a mannequin, representing a cyclist in a time-trial position, are placed on a two-component force sensor, integrated into an elevated platform equipped with a specially designed support system. The measurement setup is illustrated in Fig. 9. The mannequin was crafted using high-density polyurethane, CNC milled based on a 3D scan of an elite cyclist, which was also utilized in the CFD simulations conducted in the study. Subsequently, the mannequin underwent surface treatment for a smooth finish. The scanning process received rider consent and was approved by the Ethical Review Board of Eindhoven University of Technology under Nr. ERB2020BE_1859456_WT. The bicycle is equipped with aero-bars, a rear full disc wheel, and a front spoked wheel with sixteen bladed spokes. The total frontal area, encompassing both the cyclist and the bicycle, is 0.338 m^2 . To isolate the aerodynamic drag specific to the cyclist and bicycle, the forces on the platform, including the support structure, are independently measured ($C_{DA} = 0.030 \text{ m}^2$ at 15 m/s) and then subtracted from the overall measured drag of the entire system, assuming negligible interaction effects. The wind velocity is measured with an upstream cobra probe as shown in Fig. 9. All measurements are conducted at angle of 0° . Additionally, the results are corrected for variations in temperature, atmospheric pressure, and relative humidity during the experimental sessions, to a standard sea-level atmospheric pressure and air density of 1.225 kg/m^3 at 15°C .

4.1.2. WT results

The WT tests are conducted for three suits at six different velocities, ranging from approximately 9 to 19 m/s in 2 m/s increments, as depicted in Fig. 10. The whiskers represent a standard deviation of 0.0005 m^2 based on 30 repeated measurements conducted under similar experimental conditions at a velocity of 15 m/s.

Across all configurations, there is a consistent decrease in C_{DA} as the wind velocity increases. Among the examined wind velocities, suit 2, characterized by rough arms and back, consistently exhibits the lowest



Fig. 8. Cycling mannequin with three skinsuit zones.

Table 4

Implemented fabrics in zones 1, 2 and 3 for each suit.

	Zone 1	Zone 2	Zone 3
Suit 1	F_S	F_S	F_S
Suit 2	F_S	F_R	F_R
Suit 3	F_S	F_R	F_S

C_{DA} . Conversely, suit 3, featuring a rough back, consistently shows the highest C_{DA} at every wind velocity except 9 m/s. Specifically, at a wind velocity of 15 m/s, suit 3 experiences a 0.6 % higher drag compared to the smooth suit 1 (0.198 m^2 vs. 0.197 m^2), while suit 2 records a 5.3 % reduction in drag (0.186 m^2 vs. 0.197 m^2) compared to suit 1.

The assessment of the CFD simulations in the next subsection will be conducted at a cycling velocity of 15 m/s, denoted by the vertical dashed line in Fig. 10.

4.2. CFD skinsuit simulations

In this section, the evaluation of fabric representations through their associated k_S values is performed using CFD, with the utilization of a full skinsuit on a cycling model. The assessment takes place at a cycling velocity of 15 m/s, and the obtained drag values are validated with the WT measurements.

4.2.1. Computational geometry

The computational geometry is acquired using an Eva structured light 3D scanner and processed to generate the computational geometry illustrated with characteristic angles in Fig. 11a. Note that this scanned geometry was also used to construct the mannequin used in subsection 4.1. A TT bicycle with an open front and a disk rear wheel is used, with simplification of the computational geometry by excluding chains, cables, and spokes. The body is segmented into separate surfaces that align with the stitching pattern of the actual skinsuit (Fig. 11b). This segmentation facilitates the imposition of different roughness heights on different parts of the skinsuit. These surfaces are categorized into three zones, similar to those in the WT experiments: Zone 1 encompasses the shorts, the race number pocket, and the shoes; zone 2 includes the chest, shoulders, and arms of the skinsuit; and zone 3 comprises the back area.

4.2.2. Computational domain

The computational geometry of the cyclist and bicycle is placed in a computational domain as depicted in Fig. 12. The computational domain dimensions are determined in accordance with best practice guidelines (Franke et al., 2007; Tominaga et al., 2008; Blocken, 2015) and are set at 16 m (width) $\times 32 \text{ m}$ (length) $\times 8 \text{ m}$ (height) to minimize interference with the flow field around the cyclist. The cyclist is positioned at 5.1 m from the domain's inlet, while maintaining a 0.05 m gap between the wheels and the domain's bottom surface (Malizia and Blocken, 2020b). With a combined frontal area (A) of the cyclist and bike of 0.338 m^2 , the resulting blockage ratio is 0.27 %, which falls below the recommended maximum of 3 % as recommended by Franke et al. (2007), Tominaga et al. (2008), and Blocken (2015).

4.2.3. Computational grid and grid-sensitivity analysis

The computational grid, depicted in Fig. 13, adheres to best practice guidelines for the CFD performance of cycling aerodynamics (Malizia et al., 2019; van Druenen and Blocken, 2024). A sensitivity analysis, systematically refining both the surface grid and the near-wall volume grid, was performed to assess grid-independency. Tetrahedral-based grid typologies are used, applying triangular prism cells with a three-sided base in the boundary layer, while the volume grid is composed of tetrahedral cells. The size of triangular surface cells varies from 1 to 3 mm, determined by curvature functions. A total of 28 prism cell layers is applied to maintain a maximum prism cell layer growth rate of 1.15 and a last-ratio value of 30 % (ANSYS, 2021c). This ensures a



Fig. 9. Open-section wind tunnel setup for skinsuit tests.

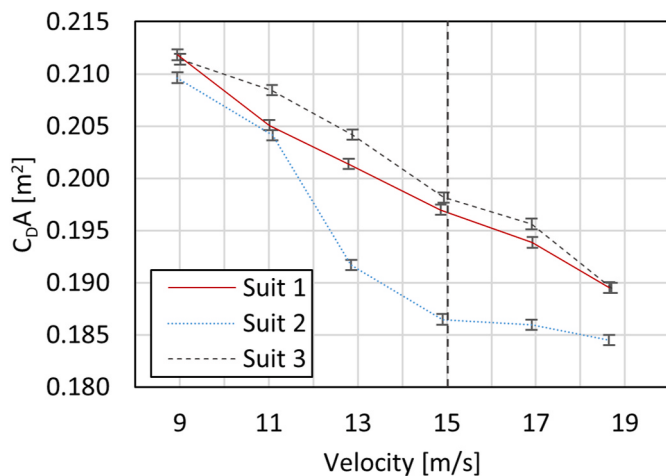
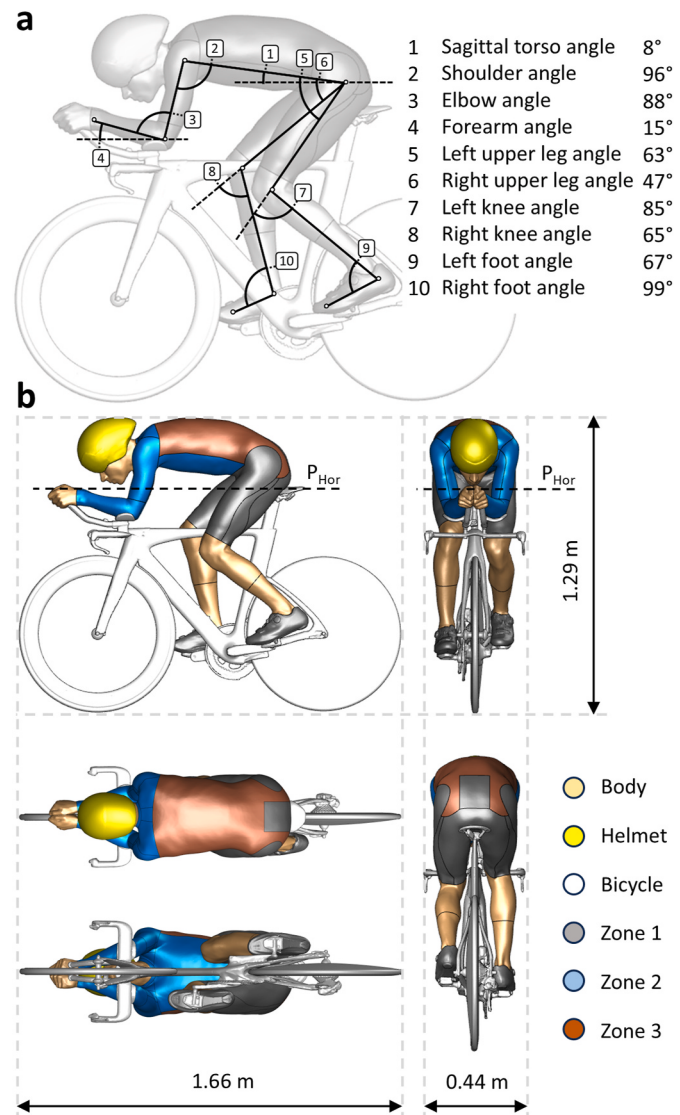


Fig. 10. Wind tunnel skinsuit test results. Whiskers represent one standard deviation.

smooth transition between the prism cells in the final near-wall grid layer and the tetrahedral cells in the volume grid. The y_p value is uniformly set to 0.01 mm, resulting in an approximate area-averaged y^+ value of 0.5. Three refinement zones are defined around the cyclist and in the wake, with maximum cell lengths of 0.01 m in W_1 , 0.02 m in W_2 , and 0.04 m in W_3 .

The grid-sensitivity analysis employs the SST $k-\omega$ model, with computational settings and boundary conditions as will be detailed in subsections 4.2.4 and 4.2.5. The assigned k_S values at the cyclists' surfaces are $k_S = 0$ mm for the helmet and bicycle surfaces, and $k_S = 0.01$ mm for zones 1, 2, and 3, as well as the body surface.

Three grids are generated, varying the minimum and maximum cell lengths. Consequently, the number of prism cell layers differs between the grids to maintain a 1.15 cell layer height growth rate and a last-ratio value of 30 %. Grid a (see Fig. 14a) is the finest, with a minimum surface cell length of 1 mm and a maximum surface cell length of 2 mm, 25 prism cell layers, and a cell count of 117,924,100 cells. Grid b (see Fig. 14b) has a minimum surface cell length of 1 mm and a maximum surface cell length of 3 mm, 28 prism cell layers, and a cell count of 93,832,539 cells. Grid c has a minimum surface cell length of 2 mm and a maximum surface cell length of 4 mm, 30 prism cell layers, and a cell count of 46,149,621 cells (see Fig. 14c). Fig. 14d displays the results of the refinement study in terms of the $C_{D,A}$. Compared to the finest grid (a), grid b exhibits an underestimation of 0.7 %, while grid c shows an underestimation of 3.8 %. Based on this evaluation, grid b is selected for

Fig. 11. Computational geometry with (a) characteristic angles and (b) surface segmentation according to skinsuit with the horizontal section plane P_{Hor} indicated.

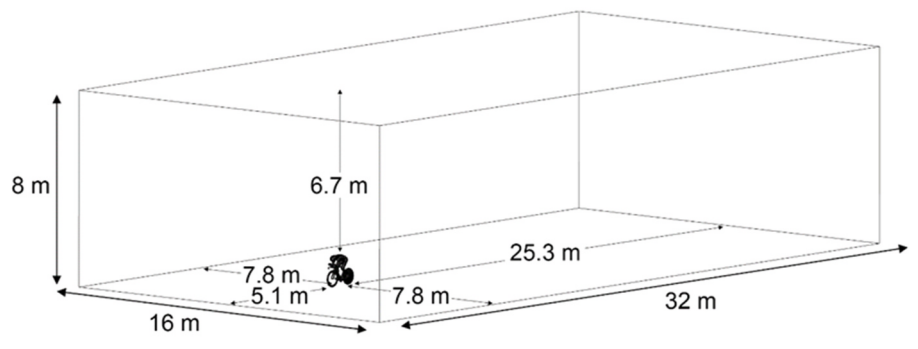


Fig. 12. Computational domain.

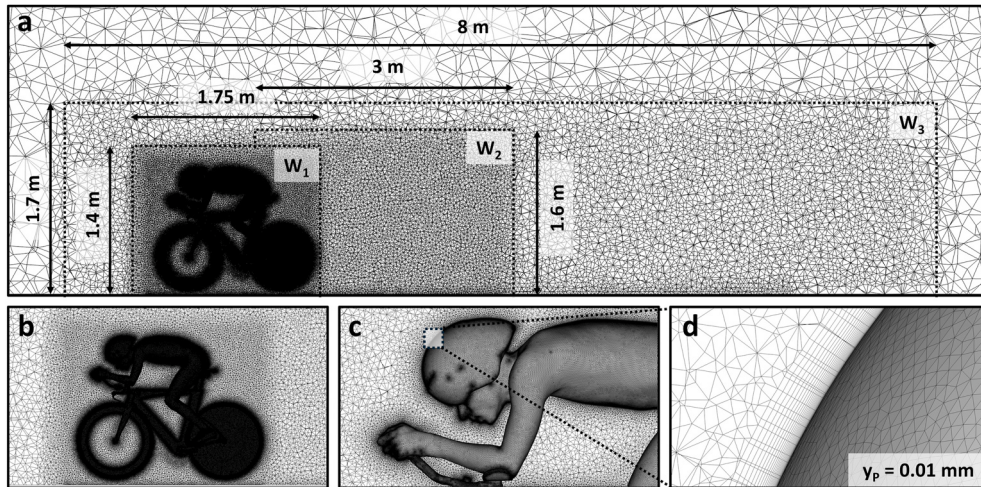


Fig. 13. Computational grid including (a-c) refinement zones and (d) near-wall prism layers.

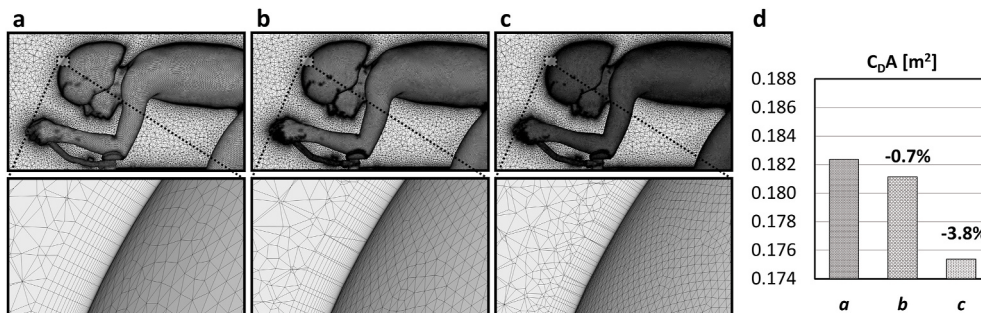


Fig. 14. (a) fine grid with 117,924,100 cells, (b) medium grid with 93,832,539 cells, (c) coarse grid with 46,149,621 cells and (d) calculated drag areas on these three grids.

the remainder of this study.

4.2.4. Computational settings

The 3D steady Reynolds-Averaged Navier-Stokes (RANS) equations are solved using ANSYS Fluent 21.1 (ANSYS, 2021b) with both the SST $k-\omega$ and T-SST model, each employing a distinct transition model, to determine the cyclist drag area. The computational settings are similar to those outlined for the 2D steady RANS equations in subsection 3.2.3. The pseudo-transient solver with automated time stepping is used, and for both methods, drag values are averaged over 5000 iterations, following an initial 1000 iterations performed for the initialization of the flow field.

4.2.5. Boundary conditions

At the domain inlet, a uniform mean velocity of 15 m/s and a turbulence intensity of 0.5 % are applied to simulate high-speed cycling in the absence of external atmospheric wind. The distinct surface zones of

Table 5
Applied k_S value per zone for each suit.

Equivalent sand-grain roughness height k_S [mm]				
	Body, helmet, bicycle	Zone 1	Zone 2	Zone 3
Suit 1	0	0.05	0.05	0.05
Suit 2	0	0.05	1/5/10	1/5/10
Suit 3	0	0.05	0.05	1/5/10

the cyclist, depicted in Fig. 11, are assigned k_s values as specified in Table 5. This allocation includes the application of $k_s = 0$ mm for the helmet, bicycle, face, hands and lower legs, while zone 1 is assigned a k_s value of 0.05 mm. The k_s values for zones 2 and 3 vary across the three suits. At the outlet, zero static gauge pressure is specified, and the lateral boundaries are slip walls.

4.3. Validation results

The results from both CFD and WT are compared based on the value of C_{DA} (Fig. 15) and the percentage drag relative to that of the mannequin wearing suit 1, which is the suit with F_s applied to zone 1, 2, and 3 of the skinsuit (Fig. 16).

Fig. 15 shows that there is a good agreement in C_{DA} within the range of -0.6 %–0.6 % when using SST $k-\omega$ and T-SST for suit 1 and suit 3, across all applied k_s values for F_R . However, both SST $k-\omega$ and T-SST models tend to overestimate the drag for suit 2. Depending on the applied k_s value for F_R , the deviation ranges between 3.3 % and 4.3 % for SST $k-\omega$ and between 1.6 % and 3.5 % for T-SST. For both turbulence models, the drag, and consequently the deviation compared to the WT measurements, decreased with using higher k_s values.

Analysing the drag change in comparison to the drag observed when wearing suit 1 (Fig. 16), the use of suit 2 results in a -5.3 % drag change in the WT experiments. However, for SST $k-\omega$, the drag change for suit 2 is limited within the range of -0.7 % to -1.7 %, showing a decreasing drag difference with higher k_s values. Similarly, with T-SST, the drag change varies from -2.5 % to -4.2 %, also displaying a decreasing drag with increasing k_s values. In both WT experiments and CFD simulations with either SST $k-\omega$ or T-SST, the use of suit 3 consistently yields higher drag values compared to suit 1. Specifically, in the WT experiments, the increase in drag is 0.6 %. Using the SST $k-\omega$ model, the drag increase varies from 0.6 % to 1 %, while employing the T-SST model results in a drag increase ranging from 0.3 % to 0.8 %.

4.4. Analysis of the CFD results

In this section, an in-depth analysis of the drag values and flow field derived from the CFD simulations is conducted to evaluate the implications of employing various k_s values at different locations on the skinsuit.

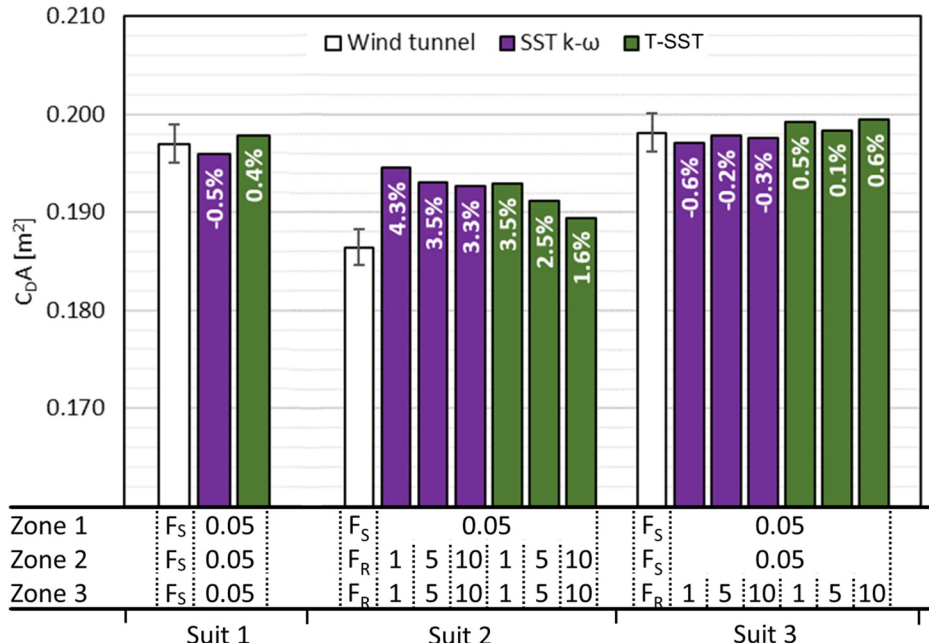


Fig. 15. Drag area per suit obtained by WT experiments and CFD simulations. Values below the x-axis denote the applied k_s value for the corresponding zones in mm.

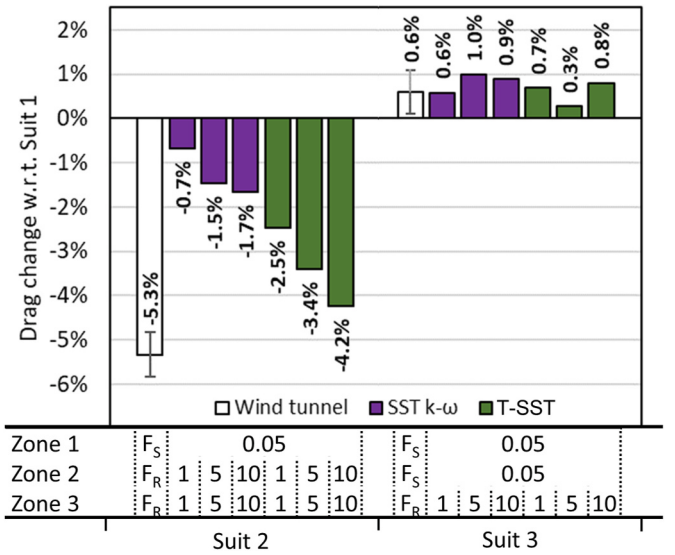


Fig. 16. Change in drag in comparison to the drag from suit 1. Values at the bottom denote the applied k_s value for the corresponding zones in mm.

The drag area C_{DA} is the integral of the static pressure (C_pA) and shear stress (C_fA) distributions across the surface of a body and aligned with the free-stream velocity direction, where

$$C_pA = \frac{2}{\rho U_c^2} \int_S n_x P dS \quad (11)$$

and P is the time-averaged pressure (Pa) distribution at the surface, n_x is the normal vector to the surface projected onto the free stream direction, S is the exterior surface, and

$$C_fA = \frac{2}{\rho U_c^2} \int_S t_x \tau_w dS \quad (12)$$

where t_x is the tangential vector to the surface projected onto the free-stream direction. Figs. 17 and 18 illustrate the contribution of C_pA and C_fA to C_{DA} for the six different zones identified in Fig. 11. The data

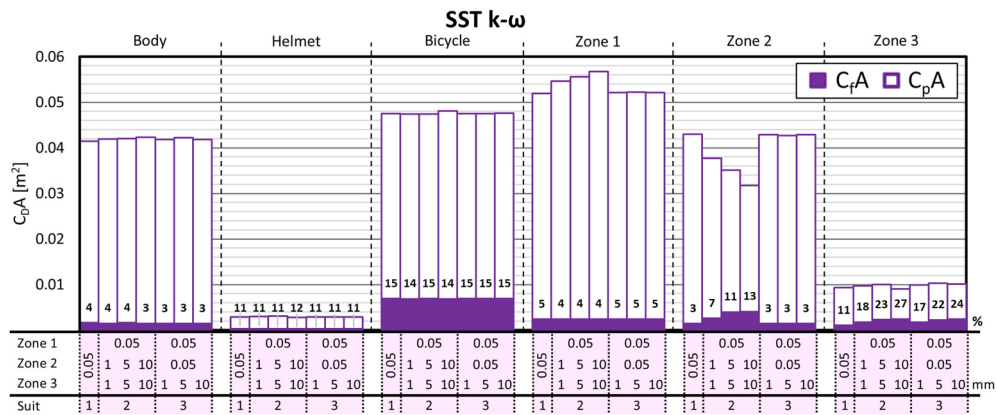


Fig. 17. Calculated drag area by SST $k\omega$ per zone including the share of both $C_f A$ and $C_p A$ where the values in the bar chart represent the percentage share of $C_f A$ to $C_d A$. The values below the x-axis denote the applied k_s value for the corresponding zones in mm.

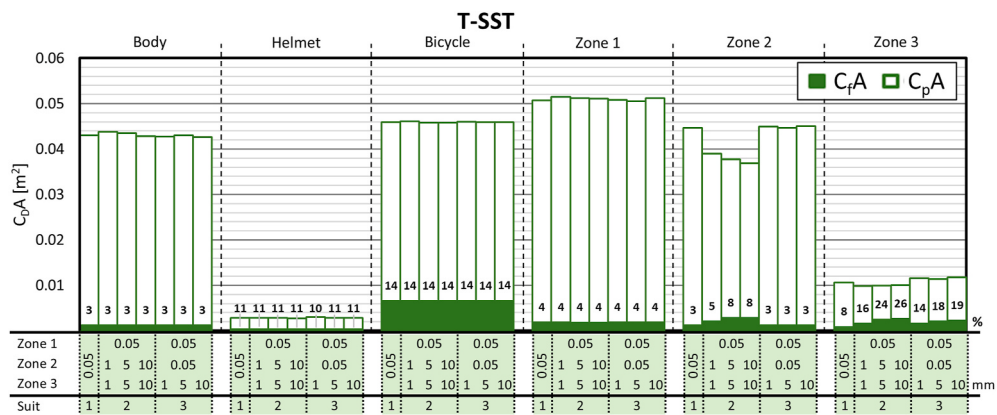


Fig. 18. Calculated drag area for T-SST per zone including the share of both $C_f A$ and $C_p A$ where the values in the bar chart represent the percentage share of $C_f A$. The values below the x-axis denote the applied k_s value for the corresponding zones in mm.

labels represent the percentage share of $C_f A$ to $C_d A$. For both SST $k\omega$ (Fig. 17) and T-SST (Fig. 18), increasing k_s in zone 2 and 3 does not result in significant changes ($>0.001 \text{ m}^2$) in the body, helmet, and bicycle zones. This holds true for zone 1 in T-SST (Fig. 18) as well. However, for SST $k\omega$ (Fig. 17), $C_d A$ in zone 1 increases with an increasing k_s value in zone 2, from 0.052 m^2 for $k_s = 0.05 \text{ mm}$ to 0.057 m^2 for $k_s = 0.10 \text{ mm}$. The ratio of $C_f A$ to $C_p A$ remains consistent.

In zone 2, the local increase in k_s is associated with a decrease in $C_d A$ as k_s grows. For SST $k\omega$, it decreases from 0.043 m^2 for $k_s = 0.05 \text{ mm}$ to 0.032 m^2 for $k_s = 0.10 \text{ mm}$, and for T-SST, it decreases from 0.045 m^2 to 0.037 m^2 . The share of $C_f A$ increases significantly from 3 % at $k_s = 0.05$

mm to 13 % at $k_s = 0.10 \text{ mm}$ for SST $k\omega$ and to 8 % at $k_s = 0.10 \text{ mm}$ for T-SST.

With a k_s value of 0, the share of $C_f A$ is relatively larger for the helmet and bicycle surfaces compared to the body surface. As depicted in Fig. 11, the body surface includes the face, hands, and lower legs. This larger share of $C_f A$ can likely be attributed to the aerodynamic design of both the helmet and bicycle, aimed at minimizing wakes and, consequently, C_p . Similarly, in zone 3, as anticipated, the share of $C_f A$ is also relatively high compared to that in zones 1 and 2, owing to its relatively parallel orientation to the main flow direction and absence of large pressure gradients.

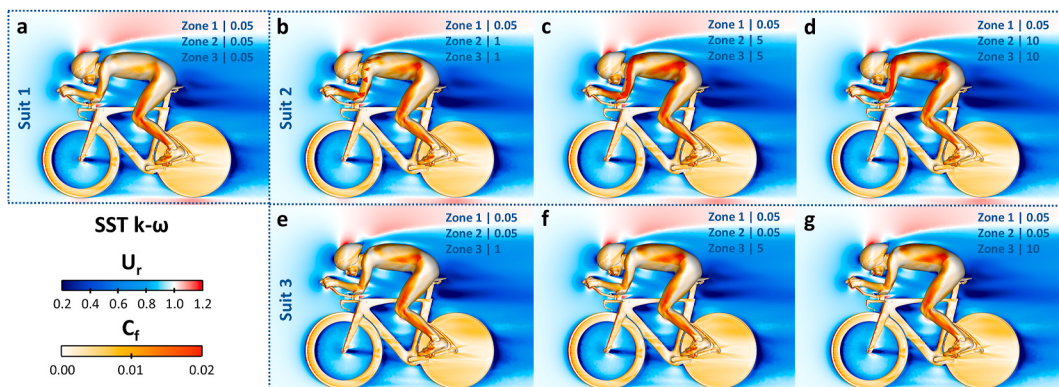


Fig. 19. Contours of U_r in the vertical centre plane and contours of C_f on the cyclist and body surfaces for (a) suit 1, (b-d) suit 2 and (e-g) suit 3, for SST $k\omega$.

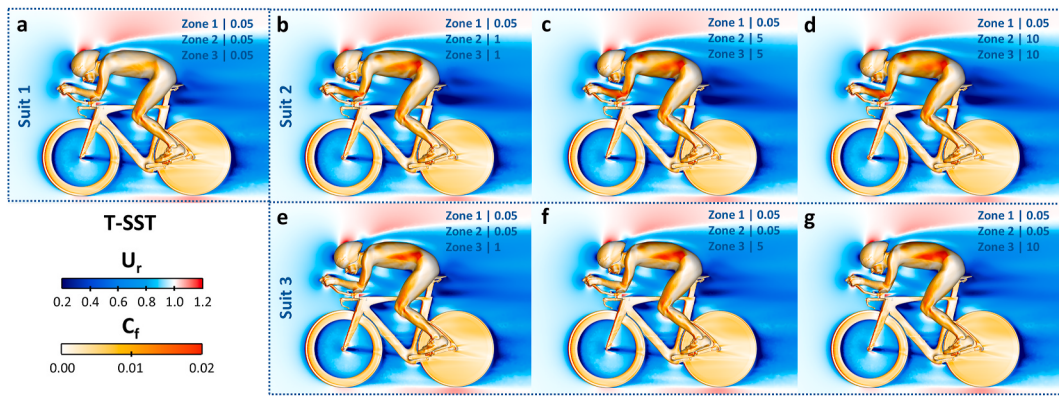


Fig. 20. Contours of U_r in the vertical centre plane and contours of C_f on the cyclist and body surfaces for (a) suit 1, (b-d) suit 2 and (e-g) suit 3, for T-SST.

Figs. 19 and 20 depict contours of the velocity ratio U_r in the vertical centre plane and contours of C_f on the cyclist and bicycle surfaces for SST $k-\omega$ and T-SST, respectively. The configurations include suit 1 (subfigure a), suit 2 (subfigures b-d), and suit 3 (subfigures e-g). The velocity ratio U_r is defined as $U_r = U/U_c$, with U representing the magnitude of the local 3D velocity vector. The skin friction coefficient C_f is defined as:

$$C_f = \frac{\tau_w}{0.5\rho U_c^2} \quad (13)$$

Contours of U_r exhibit minor differences among the various configurations. Generally, the low-velocity region (dark blue) behind the saddle is slightly larger for suit 2. This observation is remarkable, as a larger low-velocity region typically indicates higher pressure drag. However, suit 2 actually results in lower drag.

For SST $k-\omega$, C_f is highest on the sides of the leg for suit 1 (Fig. 19a), with other areas generally showing C_f values smaller than 0.01. Increasing the k_S value for suit 2 in zones 2 and 3 leads to higher C_f in these specific zones. This is noticeable on the sides of the lower and upper arms and the flank for $k_S = 1$ mm (Fig. 19b). Further increases to $k_S = 5$ mm (Fig. 19c) and $k_S = 10$ mm in zones 2 and 3 (Fig. 19d) result in more pronounced increases, reaching values exceeding $C_f = 0.02$. In suit 3, only the k_S value in zone 3 is increased compared to suit 1, leading to increased C_f , particularly in this zone. The presented side views highlight an increase in C_f in the flank (Fig. 19e–g).

For T-SST, for suit 1, lower C_f values are noted on the side of the leg (Fig. 20a) compared to SST $k-\omega$ (Fig. 19a). Additionally, the local increase in C_f by raising k_S at the upper arm is less prominent for T-SST (Fig. 20b–d). Increasing k_S in zone 3 leads to an increase in C_f (Fig. 20b–g) in the back/flank area, similar to the observed trend for SST $k-\omega$ (Fig. 19b–g).

Figs. 21 and 22 provide a detailed view of C_f distributions, along with

skin friction lines to pinpoint flow separation points. In the case of SST $k-\omega$ and suit 1, a vertically projected line of flow separation is visible on the upper arm (indicated by the dashed line in Fig. 21a). Originating from the shoulder's side centre point, this line moves downward along the upper arm toward the back side of the elbow. With an increase in the k_S value on the upper arm surfaces (zone 2), the projected line of flow separation shifts downstream towards the armpit (Fig. 21b–d). Additionally, C_f on the upper left leg increases, despite the k_S value remaining unchanged in this region. This phenomenon could be attributed to a different local approach flow, influenced by the changing wake flow behind the upper arms. Based on the current perspectives, it appears that increasing the k_S value in zone 3 does not significantly alter the skin friction lines and flow separation on the back of the cyclist. For the upper left leg, the projected line of flow separation, not explicitly depicted in Figs. 21 and 22, aligns closely with the angle of this upper leg (refer to Fig. 11) across all suits.

Similarly, for T-SST, the separation points on the upper arm shift downstream with a local increase in k_S value. At $k_S = 0.05$ (Fig. 22a–e), the line of flow separation extends from the side centre point of the shoulder to the back of the elbow. As k_S increases, the line inclines towards the armpit region. Regions with higher C_f emerge on the back side of the upper arm and on the upper arm and elbow region. In contrast to SST $k-\omega$, for T-SST, the skin friction is not significantly affected on the upper left leg when k_S is increased in zone 2 (Fig. 21a–d vs Fig. 22a–d). This observation aligns with the earlier findings in Fig. 18.

Fig. 23 presents a top view with contours of C_f on the cyclist's surface and contours of U_r , supported by 2D streamlines, at horizontal cross-section P_{Hor} through the upper arms at a height of 1 m (see Fig. 11b for P_{Hor} location). Part of the cyclist's body is made transparent to analyse the flow in the left upper arm wake region. Due to geometric asymmetry, U_r shows no symmetry in the sagittal plane. For both

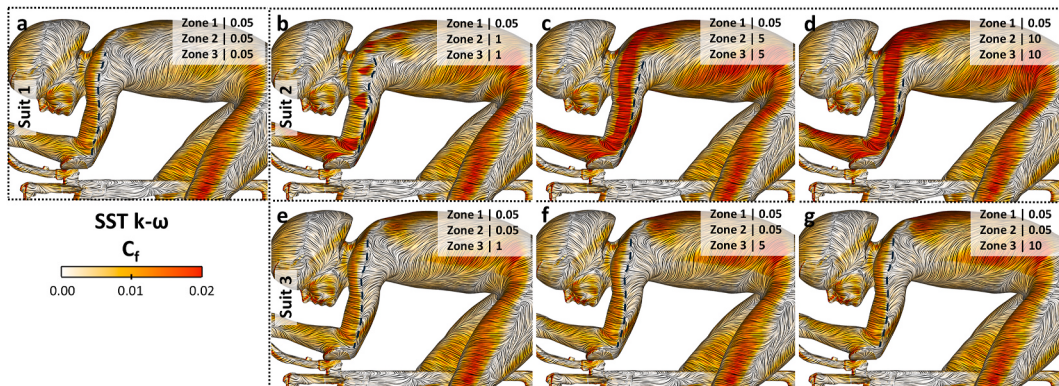


Fig. 21. Contours of C_f on the cyclist and body surfaces, overlaid with skin friction lines and dashed lines to highlight flow separation on the upper arm for (a) suit 1, (b-d) suit 2 and (e-g) suit 3, for SST $k-\omega$.

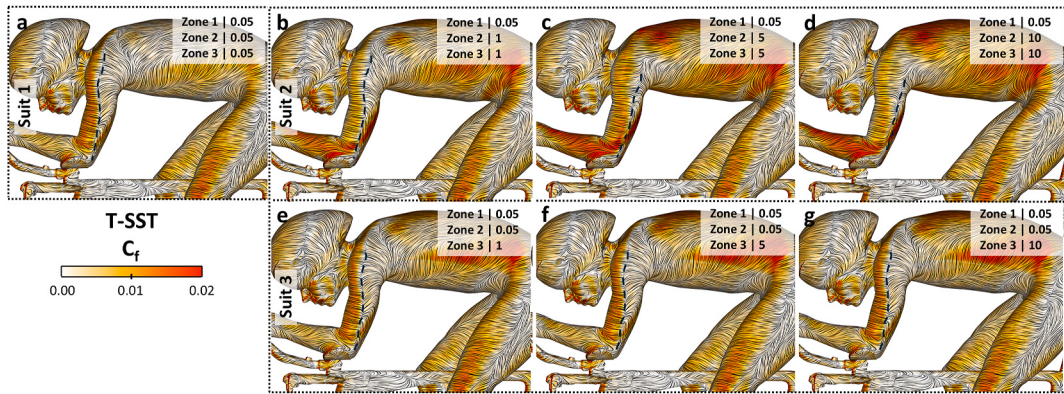


Fig. 22. Contours of C_f on the cyclist and body surfaces, overlaid with skin friction lines and dashed lines to highlight flow separation on the upper arm for (a) suit 1, (b-d) suit 2 and (e-g) suit 3, for T-SST.

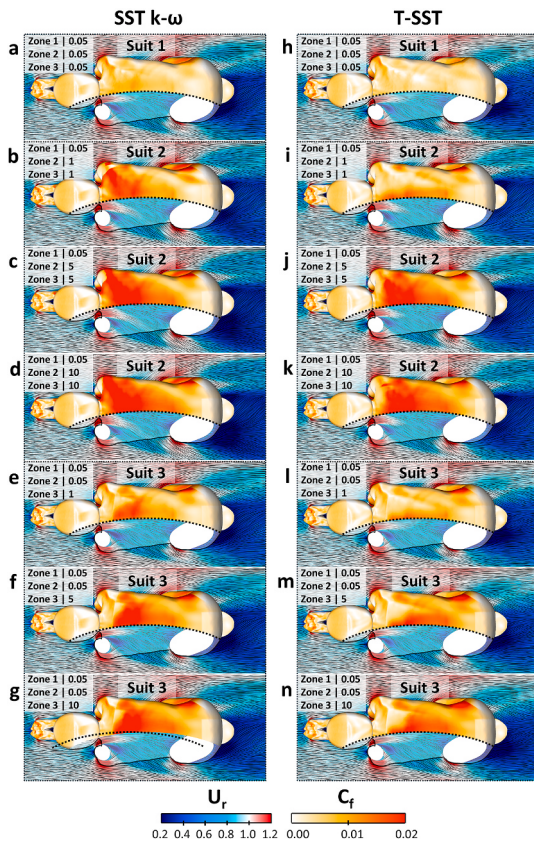


Fig. 23. Contours of U_r in horizontal plane at a height of 1 m (as indicated by $P_{H\alpha}$ in Fig. 11b) overlaid with streamlines, and contours of C_f on the cyclist and body surfaces, for (a-h) SST $k-\omega$ and (h-n) T-SST.

turbulence models, C_f increases on the back area with a local increasing k_s value. For $k_s = 0.05$ mm in all zones (suit 1, Fig. 23a–h), C_f on the back area is generally lower than 0.01. For $k_s = 1$ mm in zone 3 (suit 2 and 3, Fig. 23b–e,j,l), C_f approaches a value of 0.02 on the upper back area. For $k_s = 5$ mm (Fig. 23c–f,j,m) and $k_s = 10$ mm (Fig. 23d–g,k,n) in zone 3, C_f locally exceeds 0.02 on the upper back area. Compared to suit 3, a larger area of red is visible for suit 2 for both SST $k-\omega$ (Fig. 23b–d vs Fig. 23e–g) and T-SST (Fig. 23i–k vs Fig. 23l–n). This increase could originate from the higher back/shoulder region, which is part of zone 2. In comparison to suit 3, the k_s value in zone 2 is higher for suit 2. When comparing similar suits (Fig. 23a–g vs Fig. 23h–n), C_f is generally

slightly higher for SST $k-\omega$ than for T-SST.

For suit 2, the higher k_s value on the upper arms results in delayed flow separation (Figs. 21 and 22), confirmed by the contours of U_r for both SST $k-\omega$ (Fig. 23b–d) and T-SST (Fig. 23j–k). On the inner side of the left upper arm, the red-shaded high-velocity area bends back towards the wake area, while with a lower k_s value on the upper arms (Fig. 23a–e,h,l–n), the high-velocity area is directed away from the

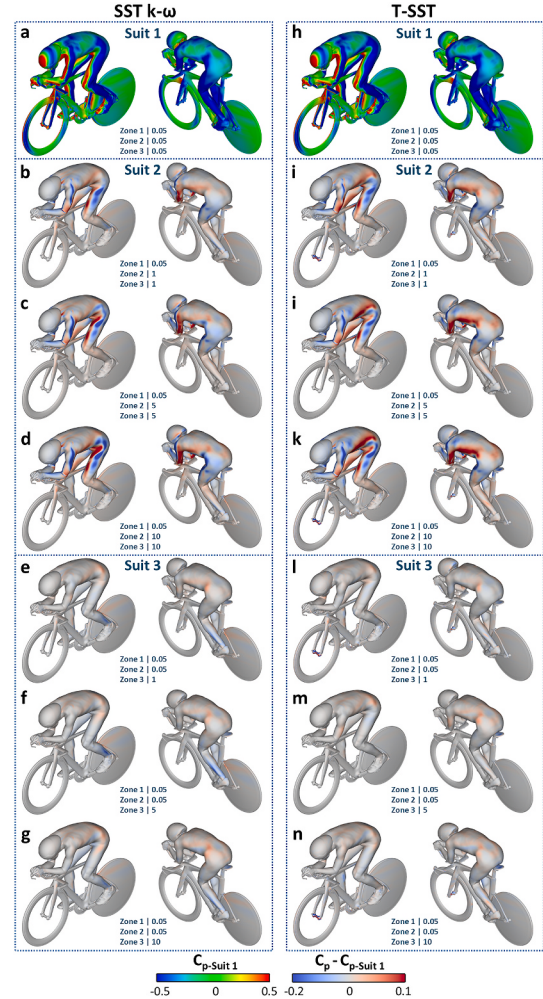


Fig. 24. Contours of (a,h) mean C_p for suit 1 and (b-g,i-n) the difference in C_p , obtained on (b-d,i-k) suit 2 and (e-g,l-n) suit 3 with respect to suit 1; for (a-g) SST $k-\omega$ and (h-n) T-SST.

wake. Consequently, the wake flow pattern around the upper arms changes, and the high-velocity areas around the upper legs increase in size.

Fig. 24a and h display contours of the pressure coefficient C_p on the cyclists' and bicycle surfaces for suit 1, utilizing SST $k-\omega$ and T-SST, respectively. The pressure coefficient is defined as:

$$C_p = \frac{(P - P_0)}{0.5\rho U_c^2} \quad (14)$$

With P_0 the freestream static pressure. These figures confirm the anticipated small pressure gradient in zone 3 (the back area), as discussed previously, contributing to an increased share of C_f in this area compared to C_p (Figs. 17 and 18).

Fig. 24b-d and i-n illustrate the differences in C_p compared to the values obtained with suit 1. These differences are presented in terms of $C_p - C_{p\text{-Suit 1}}$. In this representation, blue areas indicate a lower C_p for the corresponding suit with respect to suit 1, while red areas indicate regions where the C_p is higher.

Examining the upper left arm in Fig. 24a and d for suit 1 reveals a large blue area on the outside and back of the arm where $C_p < -0.5$. For suit 2, the k_s value is increased in this area (zone 2), resulting in a lower, more negative, C_p at the front outer side of the upper arm near the shoulder (Fig. 24b-d and i-k). This aligns with the observed increase in velocity in this region for suit 2, as shown in Fig. 23. Due to delayed flow separation and a smaller wake, a red-shaded region of higher, less negative, C_p originates at the back of the upper arms (Fig. 24b-d and i-k). This is consistent with earlier observations in cylinder studies, where the shifting of the separation point to the back of the cylinder leads to a recovery of the base pressure and thus a reduction of the drag coefficient (Achenbach, 1971).

The alteration of the upper arm wake flow could explain the difference in C_p on the upper leg. For suit 1, $C_p > 0$ is observed at the front inner side of the upper left leg, while $C_p < 0$ from the front outer side to the back of the upper left leg (Fig. 24a and d). For suit 2, a higher, more positive, C_p is observed at the front inner side of the upper leg, while lower, more negative, C_p is noted at the front outer side part of the upper leg (Fig. 24b-d and i-k). Both can be attributed to a higher-velocity approach flow due to a reduction of the upper arm wake, aligning with the observed increase in U_r around the upper legs (Fig. 23). This red area is more pronounced for SST $k-\omega$ than for T-SST, partly explaining the increase in C_{DA} in zone 1 by increasing k_s in zone 2, as previously noted in Fig. 17. The increased k_s values for suit 2 lead to a higher C_p at the body's flank, with this rise being more noticeable for T-SST (Fig. 24i-k) compared to SST $k-\omega$ (Fig. 24b-d).

Overall, it is evident that increasing the k_s value only in zone 3 (the back area) does not notably ($-0.02 < C_p - C_{p\text{-suit 1}} < 0.02$) modify the pressure distribution on the cyclist and bicycle surfaces (Fig. 24e-g, l-n).

5. Discussion

A primary challenge in modelling skinsuit roughness in CFD lies in characterizing the fabric surface roughness. In this study, fabric surface topology was not directly characterized; instead, drag reduction was assessed using cylinders covered with the fabric exposed to cross-flow conditions. This approach was applied in both WT and CFD simulations, where a range of k_s values were tested to find a match for a predetermined cycling velocity. Three cylinders, representing various limb segments of cyclists, were tested. However, a challenge emerged as no consistent k_s value could be determined for the fabrics across all three diameters. To address this, k_s values representing smooth (F_S) and rough (F_R) fabrics were determined based on the lowest Root Mean Square Error (RMSE) values. Optimal values were $k_s = 0.05$ mm (RMSE = 1.0 %) for F_S and $k_s = 5$ mm (RMSE = 11.7 %) for F_R . Additional values of $k_s = 1$ mm (RMSE = 22.4 %) and $k_s = 10$ mm (RMSE = 12.8 %) were evaluated for F_R to assess the sensitivity of k_s to both local and overall

drag.

The evaluation of the full skinsuits showcases promising agreements in drag area between WT and CFD. Notably, two out of three investigated suits exhibited very close agreements within 0.6 % using the T-SST and SST $k-\omega$ turbulence models. The third suit showed slightly larger deviations, with T-SST drag deviation from the WT drag with a 1.6 % difference and SST $k-\omega$ drag showing a 3.3 % difference. These differences are much smaller compared to the drag reductions observed on the isolated cylinders, as shown in Table 3. In those cases, drag reductions of more than 50 % were achieved by applying k_s values of up to 10 mm, compared to the smooth cylinder with $k_s = 0$. This phenomenon was also observed by Brownlie et al. (2009) in WT measurements on both cylinders and a cyclist. They assumed the cyclist to be a combination of complex tapered oval cylinders, where each cylinder affects the flow field of the others, making the flow much more complex compared to an isolated cylinder. For example, once the airflow detaches from the upper arms, it is not amenable to further surface roughness-induced flow transition. The CFD simulations in the current study enabled a more detailed examination of the flow field.

In suit 3, F_R was selectively applied only to zone 3 (back area). This resulted in a general drag increase, attributed to increased skin friction from the rough fabric application on the back; a region that is aligned for a large part approximately parallel to the flow direction and characterized by a low pressure gradient and predominantly attached flow. While the drag results showed no direct correlation between drag area (C_{DA}) and k_s value, a positive correlation was observed between k_s and the share of skin friction drag with respect to C_{DA} for both turbulence models. The impact of increasing k_s in zone 3 on the distribution of C_p was less pronounced.

In suit 2, F_R was applied to zone 2 and zone 3, covering the arms, shoulders, chest, and back. Both turbulence models provided a negative correlation between C_{DA} and the k_s value; as k_s increased, C_{DA} decreased. The drag reduction was more pronounced with the T-SST model, aligning closely with WT measurements. The lower overall reduction in C_{DA} for SST $k-\omega$ was attributed to an increase in C_{DA} in zone 1 with increasing k_s value in zone 2, limiting the overall C_{DA} reduction. Both methods showed a local decrease in C_{DA} with increasing k_s value in zone 2, accompanied by an increase in the share of C_f in C_{DA} . This decrease in C_{DA} was more pronounced for SST $k-\omega$, where C_f increased on both upper and lower arms. In contrast, for T-SST, CFD mainly showed an increase in skin friction on the lower arms, parallel to the main flow direction. Increasing k_s delayed separation on the upper arms, aligning with Terra et al. (2020), who suggested that applying roughness to this region could lower the critical velocity (U_{crit}) towards U_c . The slight increase in skin friction was compensated by a more substantial decrease in pressure drag, resulting from a smaller wake size and better pressure recovery in the wake.

These observations align with earlier findings from WT tests where rough fabrics on limb segments anticipated flow transition, reducing drag, while smooth fabrics on body segments aligned with the flow direction minimized skin friction (Kyle et al., 2004; Brownlie et al., 2009). In the current study, changes in the upper arm wake flow could explain differences in the pressure coefficient (C_p) on the upper leg. This aspect was more pronounced for SST $k-\omega$, potentially explaining the increase in C_{DA} in zone 1 due to the increasing k_s in zone 2.

Technically, the assessed skinsuit has the potential to be divided into more zones than the three examined in this study. This approach would enable a more targeted application of roughness and potentially yield a higher overall drag reduction. A novel strategy involves reversing the workflow for enhanced drag reductions: initially, conducting CFD simulations for the full skinsuit to determine an optimized set of k_s values minimizing the overall drag area (C_{DA}). Subsequently, numerically evaluating the drag reduction of these k_s values on cylinders and comparing the results with a database that includes drag reduction properties for various fabrics. This approach allows for a personalized skinsuit design, eliminating the need for time- and cost-intensive WT

testing for each rider.

The study limitations are briefly addressed. The CFD simulations employed low turbulence approach flow conditions, mirroring WT measurements, a common practice in TT cycling aerodynamics (Blocken et al., 2013, 2018b; Terra et al., 2020). Nonetheless, it is essential to recognize that low turbulence levels may not consistently reflect real-world conditions (Brown et al., 2023). Therefore, it is recommended that future studies explore the effectiveness of the workflow under moderate to high turbulence levels and assess whether the optimized designs hold up in actual racing scenarios. Future work should test the robustness of these designs under more dynamic conditions, including variable yaw angles and side forces.

To control computational costs and minimize uncertainties, certain elements were excluded, such as crosswinds and the rotation of bicycle wheels. The legs were static with the feet at about equal height. This approach aligns with one of the primary current methods of skinsuit testing, where suits are evaluated in WT testing on a static mannequin, allowing for direct comparison. The position of the legs is not expected to significantly impact the flow field around the upper body parts such as the arms, torso, and back, since previous research (Crouch et al., 2016; Griffith et al., 2019; Javadi, 2022) has shown that cyclist pedalling has a relatively limited impact on the time-averaged wake flow field. Additionally, overall drag values were found to be similar across different leg positions for a given posture (Wang et al., 2022). However, the results indicate that the distribution of aerodynamic forces, such as skin friction drag on the torso, can vary with leg position (Wang et al., 2022). Future research should therefore investigate the extent to which leg movement affects skinsuit design. Similarly, the absence of a moving floor was deemed negligible based on the measured boundary-layer height of only 40 mm on the elevated platform in the WT.

The study focused on a specific cyclist in TT posture, with the proposed workflow anticipated to be generally independent of specific cyclist characteristics. Future work is encouraged for evaluating the workflow with different cyclist models. The computational geometry did not consider small components, assuming their negligible impact.

In this study, the effect of surface roughness on the boundary layer was investigated using k_s , which, using the applied code, adjusts near-wall turbulence quantities and indirectly influences flow separation and reattachment behaviour. However, the applied γ -transition and $\gamma\text{-Re}_0$ transition models include an additional feature that allows for the specification of geometric roughness height and, based on empirical correlations, directly influences the transition location. In addition, the literature review in Section 1 indicated that no single roughness length scale could accurately represent all roughness types across different flow regimes. This challenge was also evident in the current study, where no consistent k_s value could be identified for the fabrics across all three cylinder diameters. As a result, the selection was based on the RMSE reflecting the level of agreement across all three cases. However, only three samples were available for the RMSE calculation, making the outcome potentially sensitive to outliers. While a good fit was achieved for the two tested fabrics, chosen for their directionally homogeneous structure, this limited scope restricts broader generalization. Materials such as trip strips and zigzag tapes (Timmer and Veldhuis, 2021) are known to be effective mainly for specific flow directions, making it difficult to directly translate drag reduction observed on cylinders to the complex, multi-directional flow around a complete skinsuit. Additionally, in this study, the choice of fabrics and their analysis in Section 3.1 were primarily based on the roughness element height k , while other properties, such as roughness distribution, seams, and porosity, also influence flow transition in the boundary layer. Therefore, it is recommended to expand the investigation to a wider range of fabrics and to assess the influence of both fabric properties and seam placement on the applicability of using k_s , or other roughness parameters, within the proposed workflow.

Moreover, the use of 2D steady-state RANS simulations to model the inherently unsteady flow around a cylinder is a known limitation. In this

study, this approach was considered acceptable since the primary focus was on estimating drag reduction performance to be later applied to a more complex geometry, rather than on a detailed analysis of cylinder wake behaviour. Nonetheless, scale-resolving CFD methods such as LES or hybrid RANS-LES could provide further insight into cylinder and cycling aerodynamics, and future work should evaluate the feasibility and performance of the proposed workflow using these advanced approaches.

Despite these limitations, this study has provided an integrated WT and CFD workflow to optimizing cycling skinsuit design. The good agreements found between WT and CFD simulations highlight the potential of this workflow in designing rider-specific skinsuits, encouraging further research in this area.

6. Conclusion

This work explores the use of CFD in designing cycling skinsuits. Traditionally, advanced cycling skinsuits are designed with various fabrics for zonal-specific drag reduction and undergo a costly and time-consuming development process and wind tunnel assessment. While CFD offers an alternative for performance prediction and a feasible option for rider-specific skinsuit design, accurately modelling fabric roughness poses a significant challenge. In this work the fabrics constituting the skinsuit are characterized by a k_s value based on drag reduction observed on cylinders covered with specific fabrics in both environments. Subsequently, three skinsuits, crafted from these fabrics, undergo assessment on a full-scale model. The following conclusions could be made.

6.1. Conclusions concerning the roughness correlation on cylinders

- A root mean square error (RMSE) of 1.0 % is obtained in the characterization of the smooth fabric for three cylinder diameters, comparing the drag reduction achieved in CFD using $k_s = 0.05$ mm with the drag reduction achieved in the wind tunnel.
- For the rough fabric it is more challenging to identify a single k_s value that accurately predicts the drag reduction on all three tested cylinders. The lowest RMSE of 11.7 % was found with a k_s value of 5 mm.

6.2. Conclusions concerning the roughness correlation on full skinsuits

- For suit 1 and 3, using the T-SST and SST $k\text{-}\omega$ turbulence models, the calculated drag area is within 0.6 % of the WT results.
- For suit 2, T-SST approaches the WT drag with a 1.6 % difference, while for SST $k\text{-}\omega$, this difference is 3.3 %.

6.3. Conclusions obtained from the CFD simulations on full skinsuits

- The application of higher k_s values to zone 2, including the shoulders, lower and upper arms, leads to lower drag in this zone by a downstream shift of the separation points to the back side of the upper arm, yielding a narrower wake and a better pressure recovery in the wake. The distribution of C_p is affected locally and on the surfaces in the wake of the upper arms.
- The application of high k_s values ($k_s = 1, 5$ and 10 mm) to zone 3, the back area, leads to an increase in total drag in the range of 0.3–1 %, compared to a low k_s value of 0.05 mm. This increase is due to an increase in skin friction.
- For both zone 2 and zone 3, the share of the skin friction coefficient to the local drag increases with increasing k_s value.
- The distribution of C_p on the body and bicycle is not significantly (<0.02) affected by increasing k_s in zone 3, the back area.

The agreement obtained between wind tunnel and CFD simulations emphasize the potential of employing this methodology to create

skinsuits, aerodynamically optimized to individual riders, facilitated by CFD. Further research is advised to enhance and validate this approach, encompassing riders with diverse postures and positions, and exploring a broader range of fabrics.

CRediT authorship contribution statement

Thijs van Druenen: Writing – original draft, Visualization, Validation, Methodology, Investigation, Formal analysis. **Bert Blocken:** Writing – review & editing, Supervision, Conceptualization.

Declaration of competing interest

The authors declare the following financial interests/personal relationships which may be considered as potential competing interests: T. van Druenen reports equipment, drugs, or supplies were provided by Visma Lease a bike. T. van Druenen reports equipment, drugs, or supplies was provided by Sportconfex. The second author is a member of the editorial board of the journal and should not be involved in the double-blind peer-review process. If there are other authors, they declare that they have no known competing financial interests or personal relationships that could have appeared to influence the work reported in this paper.

Acknowledgements

The authors acknowledge the partnership with Ansys CFD and extend their gratitude to the Jumbo — Visma (Visma | Lease-a-Bike) cycling team for providing cycling equipment. Special thanks are also extended to AGU and Sportconfex for supplying the fabrics and assembling the sleeves and skinsuits. This work was partially conducted on the Dutch national e-infrastructure with the support of SURF Cooperative (Grant no. EINF-13152).

Data availability

The authors do not have permission to share data.

References

- Achenbach, E., 1968. Distribution of local pressure and skin friction around a circular cylinder in cross-flow up to $re = 5 \times 10^6$. *J. Fluid Mech.* 34 (4), 625–639.
- Achenbach, E., 1971. Influence of surface roughness on the cross-flow around a circular cylinder. *J. Fluid Mech.* 46 (2), 321–335.
- ANSYS, 2021a. Fluent Theory Guide 21R1. ANSYS, Inc, Canonsburg, PA.
- ANSYS, 2021b. Fluent User's Guide 21R1. ANSYS, Inc, Canonsburg, PA.
- ANSYS, 2021c. Fluent Meshing User's Guide 21R1. ANSYS, Inc, Canonsburg, PA.
- Barry, N., Burton, D., Sheridan, J., Thompson, M., Brown, N.A.T., 2015. Aerodynamic performance and riding posture in road cycling and triathlon. *Proc. Inst. Mech. Eng. P J. Sports Eng. Technol.* 229, 28–38.
- Blocken, B., Defraeye, T., Koninckx, E., Carmeliet, J., Hespel, P., 2013. CFD simulations of the aerodynamic drag of two drafting cyclists. *Comput. Fluids* 71, 435–445.
- Blocken, B., 2015. Computational fluid dynamics for urban physics: importance, scales, possibilities, limitations and ten tips and tricks towards accurate and reliable simulations. *Build. Environ.* 91, 219–245.
- Blocken, B., van Druenen, T., Toparlar, Y., Andrianne, T., 2018a. Aerodynamic analysis of different cyclist hill descent positions. *J. Wind Eng. Ind. Aerod.* 181, 27–45.
- Blocken, B., Toparlar, Y., van Druenen, T., Andrianne, T., 2018b. Aerodynamic drag in cycling team time trials. *J. Wind Eng. Ind. Aerod.* 182, 128–145.
- Blocken, B., Gillmeier, S., Malizia, F., van Druenen, T., 2021. Impact of a motorcycle on cyclist aerodynamic drag in parallel and staggered arrangements. *Sports Eng.* 24 (Art. 7).
- Blocken, B., Malizia, F., 2024. How much can roof-mounted bicycles on a following team car reduce cyclist drag? *J. Wind Eng. Ind. Aerod.* 249, 105723.
- Blocken, B., Malizia, F., van Druenen, T., 2024. CFD analysis of chest fairings in time trial cycling. *J. Wind Eng. Ind. Aerod.* 248, 105709.
- British Cycling, 2018. Inside cervélo: part 1. <https://www.britishcycling.org.uk/knowledge/experts/ask-experts/article/20180926-Inside-Cervelo—Part-1-0>.
- Brown, C., Burton, D., Crouch, T.N., Thompson, M.C., 2023. The influence of turbulence on cycling aerodynamics. *J. Wind Eng. Ind. Aerod.* 242, 105575.
- Brownlie, L.W., 1992. Aerodynamic Characteristics of Sports Apparel. Simon Fraser University, Canada. PhD Thesis.
- Brownlie, L.W., Gartshore, I., Chapman, A., Banister, E.W., 1991. The aerodynamics of cycling apparel. *Cycl. Sci.* 44–50.
- Brownlie, L., Kyle, C., Carbo, J., Demarest, N., Harber, E., MacDonald, R., Nordstrom, M., 2009. Streamlining the time trial apparel of cyclists: the nike swift spin project. *Sports Technol.* 2, 53–60.
- Casey, M., Wintergerste, T., 2000. Ercofatc - Special interest group on "Quality and trust in industrial CFD" - best practice guidelines. European Research Community on Flow, Turbulence and Combustion.
- Cebeci, T., Bradshaw, P., 1977. Momentum Transfer in Boundary Layers. Hemisphere, Washington DC, pp. 319–321.
- Chan, L., MacDonald, M., Chung, D., Hutchins, N., Ooi, A., 2015. A systematic investigation of roughness height and wavelength in turbulent pipe flow in the transitionally rough regime. *J. Fluid Mech.* 771, 743–777.
- Chowdhury, H., Alam, F., Subic, A., 2010. Aerodynamic performance evaluation of sports textile. *Procedia Eng.* 2, 2517–2522.
- Chowdhury, H., 2012. Aerodynamics of Sports Fabrics and Garments. RMIT University, Melbourne.
- Chung, D., Hutchins, N., Schultz, M.P., Flack, K.A., 2022. Predicting the drag of rough surfaces. *Annu. Rev. Fluid Mech.* 53, 439–471.
- Chowdhury, H., Alam, F., 2014. An experimental investigation on the aerodynamic drag coefficient and surface roughness properties of sport textiles. *J. Text. Inst.* 105 (4), 414–422.
- Crouch, T.N., Burton, D., Brown, N.A.T., Thompson, M.C., Sheridan, J., 2014. Flow topology in the wake of a cyclist and its effect on aerodynamic drag. *J. Fluid Mech.* 748, 5–35.
- Crouch, T.N., Burton, D., Thompson, M.C., Brown, N.A.T., Sheridan, J., 2016. Dynamic leg-motion and its effect on the aerodynamic performance of cyclists. *J. Fluid Struct.* 65, 121–137.
- Crouch, T.N., Burton, D., LaBry, Z.A., Blair, K.B., 2017. Riding against the wind: a review of competition cycling aerodynamics. *Sports Eng.* 20, 81–110.
- Davis, J., 2022. Designing for speed. <https://blog.trekbikes.com/en/2022/06/30/designing-for-speed/>.
- Defraeye, T., Blocken, B., Koninckx, E., Hespel, P., Carmeliet, J., 2010. Aerodynamic study of different cyclist positions: CFD analysis and full-scale wind-tunnel tests. *J. Biomech.* 43, 1262–1268.
- Fage, A., Warsap, J.H., 1929. The effects of turbulence and surface roughness on the drag of a circular cylinder. *Aeronaut. Res. Coun. London, Rep. and Memo.* (1283).
- Flack, K.A., Schultz, M.P., 2014. Roughness effects on wall-bounded turbulent flows. *Phys. Fluids* 26, 101305.
- Flack, K.A., Chung, D., 2022. Important parameters for a predictive model of k_s for zero-pressure-gradient flows. *AIAA J.* 60 (10), 5923–5931.
- Forooghi, P., Stroh, A., Magagnato, F., Jakirlic, S., Frohnafel, B., 2017. Toward a universal roughness correlation. *J. Fluid Eng.* 139 (12), 121201.
- Franke, J., Hellsten, A., Schlinzen, H., Carissimo, B., 2007. Best practice guideline for the CFD simulation of flows in the urban environment. COST Action 732, Quality Assurance and Improvement of Microscale Meteorological Models. Hamburg, Germany.
- Grappe, F., Candau, R., Belli, A., Rouillon, J.D., 1997. Aerodynamic drag in field cycling. *Ergonomics* 40, 1299–1311.
- Griffith, M.D., Crouch, T.N., Thompson, M.C., Burton, D., Sheridan, J., Brown, N.A., 2014. Computational fluid dynamics study of the effect of leg position on cyclist aerodynamic drag. *J. Fluid Eng.* 136 (10), 101105.
- Griffith, M.D., Crouch, T.N., Burton, D., Sheridan, J., Brown, N.A., Thompson, M.C., 2019. A numerical model for the time-dependent wake of a pedalling cyclist. *Proc. Inst. Mech. Eng. P J. Sports Eng. Technol.* 233 (4), 514–525.
- Hama, F.R., 1954. Boundary-layer characteristics for smooth and rough surfaces. *Trans. Soc. Nav. Archit. Mar. Eng.* 62, 338–358.
- Hsu, X.Y., Miau, J.J., Tsai, J.H., Tsai, Z.X., Lai, Y.H., Ciou, Y.S., Shen, P.T., Chuang, P.C., Wu, C.M., 2019. The aerodynamic roughness of textile materials. *The Journal of the Textile Institute* 110 (5), 771–779.
- Hoerner, S.F., 1965. Fluid Dynamic Drag. Published by the author, New York, USA.
- Javadi, A., 2022. Aerodynamic study of the pedalling of a cyclist with a transitional hybrid RANS-LES turbulence model. *Flow Turbul. Combust.* 108 (3), 717–738.
- Jouybari, M.A., Yuan, J., Brereton, G.J., Murillo, M.S., 2021. Data-driven prediction of the equivalent sand-grain height in rough-wall turbulent flows. *J. Fluid Mech.* 912, A8.
- Jux, C., Sciacchitano, A., Schneiders, J.F.G., Scarano, F., 2018. Robotic volumetric PIV of a full-scale cyclist. *Exp. Fluid* 59, 74.
- Kadivar, M., Tormey, D., McGranahan, G., 2021. A review on turbulent flow over rough surfaces: fundamentals and theories. *International Journal of Thermofluids*, 100077.
- Kyle, C.R., Burke, E.R., 1984. Improving the racing bicycle. *Mech. Eng.* 34–45.
- Kyle, C.R., Brownlie, L.W., Harber, E., MacDonald, R., Nordstrom, M., 2004. The nike swift spin cycling project: reducing the aerodynamic drag of bicycle racing clothing by using zoned fabrics. *Eng. Sport* 5 (1), 118–124.
- Lee, S., Yang, J., Forooghi, P., Stroh, A., Bagheri, S., 2022. Predicting drag on rough surfaces by transfer learning of empirical correlations. *J. Fluid Mech.* 933, A18.
- Lukes, R.A., Chin, S.B., Haake, S.J., 2005. The understanding and development of cycling aerodynamics. *Sports Eng.* 8, 59–74.
- Malizia, F., Montazeri, H., Blocken, B., 2019. CFD simulations of spoked wheel aerodynamics in cycling: impact of computational parameters. *J. Wind Eng. Ind. Aerod.* 194, 103988. Article.
- Malizia, F., Blocken, B., 2020a. Bicycle aerodynamics: history, state-of-the-art and future perspectives. *J. Wind Eng. Ind. Aerod.* 200, 104134.
- Malizia, F., Blocken, B., 2020b. CFD simulations of an isolated cycling spoked wheel: impact of the ground and wheel/ground modeling. *Eur. J. Mech. B Fluid* 82, 21–38.
- Malizia, F., Blocken, B., 2021. Cyclist aerodynamics through time: better, faster, stronger. *J. Wind Eng. Ind. Aerod.* 214, 104673.

- Mebarek, A.M., Bourebia, M., Laouar, L., Bouchelaghem, N., 2024. Effect of ball burnishing process on surface roughness and corrosion behavior of S235JR steel. *Int. J. Adv. Manuf. Technol.* 130, 3431–3444.
- Menter, F.R., 1994. Eddy viscosity transport equations and their relation to the k- ϵ model. *AIAA J.* 32 (4), 632–639.
- Menter, F.R., Langtry, R.B., Likki, S.R., Suzen, Y.B., Huang, P.G., Völker, S., 2006a. A correlation-based transition model using local Variables—Part I: model formulation. *J. Turbomach.* 128 (3), 413–422.
- Menter, F.R., Langtry, R., Völker, S., 2006b. Transition modelling for general purpose CFD codes. *Flow Turbul. Combust.* 77 (1–4), 277–303.
- Menter, F.R., Smirnov, P.E., Liu, T., Avancha, R., 2015. A one-equation local correlation-based transition model. *Flow Turbul. Combust.* 95, 583–619.
- Moria, H.A., 2013. Experimental Study of Aerodynamic Behaviour of Stretchable Sport Fabrics. RMIT University, Melbourne.
- Nikuradse, J., 1933. Laws for flows in rough pipes. *VDI-Forschungsh* 361.
- Oggiano, L., Sætran, L., Løset, S., Winther, R., 2007. Reducing the athlete's aerodynamical resistance. *J. Comput. Appl. Mech.* 8, 2007.
- Oggiano, L., Sætran, L.R., 2009. Experimental analysis on parameters affecting the drag force on athletes. *Impact Technology Sport* 3, 383–389.
- Oggiano, L., Konopov, I., Troynikov, O., Alam, F., Subic, A., 2009a. Aerodynamic behaviour of single sport Jersey fabrics with different roughness and cover factors. *J. Sport Eng.* 12, 1–16.
- Oggiano, L., Konopov, I., Troynikov, O., Alam, F., Subic, A., Sætran, L.R., 2009b. Aerodynamic and comfort properties of single Jersey textiles for high-speed sports. *Impact Technology Sport* 3, 167–173.
- Oggiano, L., 2010. Drag Reduction and Aerodynamic Performances in Olympic Sports. Norwegian University of Science and Technology, Trondheim.
- Oggiano, L., Brownlie, L., Troynikov, O., Bardal, L.M., Sæter, C., Sætran, L.R., 2013. A review on skin suits and sport garment aerodynamics: guidelines and state of the art. *Procedia Eng.* 91, 91–98.
- Rezaeiha, A., Kalkman, I., Blocken, B., 2017. CFD simulation of a vertical axis wind turbine operating at a moderate tip speed ratio: guidelines for minimum domain size and azimuthal increment. *Renew. Energy* 107, 373–385.
- Rezaeiha, A., Montazeri, H., Blocken, B., 2018. Towards accurate CFD simulations of vertical axis wind turbines at different tip speed ratios and solidities: guidelines for azimuthal increment, domain size, and convergence. *Energy Convers. Manag.* 156, 301–316.
- Schlichting, H., 1936. Experimental Investigation of the Problem of Surface Roughness, VII. *Ing.-Arch.*
- Spoelstra, A., de Martino Norante, L., Terra, W., et al., 2019. On-site cycling drag analysis with the ring of fire. *Exp. Fluid* 60, 90.
- Tominaga, Y., Mochida, A., Yoshie, R., Kataoka, H., Nozu, T., Yoshikawa, M., Shirasawa, T., 2008. AIJ guidelines for practical applications of CFD to pedestrian wind environment around buildings. *J. Wind Eng. Ind. Aerod.* 96 (10–11), 1749–1761.
- Terra, W., Sciacchitano, A., Scarano, F., 2020. Cyclist reynolds number effects and drag crisis distribution. *J. Wind Eng. Ind. Aerod.* 200, 104143.
- Thakkar, M., Busse, A., Sandham, N., 2017. Surface correlations of hydrodynamic drag for transitionally rough engineering surfaces. *J. Turbul.* 18 (2), 138–169.
- Timmer, N., Veldhuis, L., 2021. The impact of skinsuit zigzag tape turbulators on speed skating performance. *Appl. Sci.* 11 (988).
- Underwood, L., Jeremy, M.C., 2011. Fabric testing for cycling skinsuits. In: Proceedings of the 5th Asia-Pacific Congress on Sports Technology (APCST), pp. 350–356.
- Union Cycliste Internationale, 2024. UCI Cycling Regulations: General Organisation of Cycling as a Sport. Version on 01.04.2024).
- van Druenen, T., Blocken, B., 2023. Aerodynamic impact of cycling postures on drafting in single paceline configurations. *Comput. Fluid* 257. Article 105863.
- van Druenen, T., Blocken, B., 2024. CFD simulations of cyclist aerodynamics: impact of computational parameters. *J. Wind Eng. Ind. Aerod.* 248, 105714.
- Wang, S., Pitman, J., Brown, C., Tudball Smith, D., Crouch, T., Thompson, M.C., Burton, D., 2022. The influence of the inter-relationship of leg position and riding posture on cycling aerodynamics. *Fluid* 7 (1), 18.
- Yang, J., Stroh, A., Lee, S., Bagheri, S., Frohnafel, B., Forooghi, P., 2023. Prediction of equivalent sand-grain size and identification of drag-relevant scales of roughness – a data-driven approach. *J. Fluid Mech.* 975, A34.
- Zdravkovich, M.M., Ashcroft, M.W., Chisholm, S.J., Hicks, N., 1996. Effect of cyclist's posture and vicinity of another cyclist on aerodynamic drag. In: Haake, S.J. (Ed.), *The Engineering of Sport*, pp. 21–28.
- Zdravkovich, M.M., 1997. *Flow Around Circular Cylinders: Volume I: Fundamentals*. OUP, Oxford.